



Ventricular segmentation and modeling using topological watershed transformation and harmonic state model

Ramzi Mahmoudi

► To cite this version:

Ramzi Mahmoudi. Ventricular segmentation and modeling using topological watershed transformation and harmonic state model. International Journal of Imaging Systems and Technology, 2022, 10.1002/ima.22818 . hal-03836924

HAL Id: hal-03836924

<https://hal.science/hal-03836924>

Submitted on 2 Nov 2022

HAL is a multi-disciplinary open access archive for the deposit and dissemination of scientific research documents, whether they are published or not. The documents may come from teaching and research institutions in France or abroad, or from public or private research centers.

L'archive ouverte pluridisciplinaire **HAL**, est destinée au dépôt et à la diffusion de documents scientifiques de niveau recherche, publiés ou non, émanant des établissements d'enseignement et de recherche français ou étrangers, des laboratoires publics ou privés.

Ventricular Segmentation and Modeling Using Topological Watershed Transformation and Harmonic State Model

Ramzi Mahmoudi ^{1,2,*}

¹ University of Monastir - Laboratory of Medical Imaging Technology - LTIM-LR12ES06, Faculty of Medicine of Monastir - 5019 Monastir, Tunisia

² University of Paris-Est, Computer Science Laboratory Gaspard-Monge, Mixed Unit CNRS-UMLV-ESIEE UMR8049, ESIEE Paris, 93162 Noisy Le Grand, France

* Correspondence: ramzi.mahmoudi@esiee.fr

Abstract: This paper proposes an adapted ventricular segmentation method based on topological watershed transform. Segmentation will allow spatio-temporal modeling of trajectories of the different points belonging to the borders of the ventricle using a harmonic motion model that is able to describe such motion over the entire cardiac cycle. In addition, extraction of the adopted canonical state vector and the corresponding state equations guarantees an optimal efficacy and a gradual transition from order n to order $n+1$. To validate the proposed approach, an intern-image base was used. Our results show a promising ability to discern whether subjects are healthy or pathological with an 80% success rate.

Keywords: Cardiac, MRI, Right ventricle, Segmentation, Topological, Watershed, Modeling, Harmonic model, Kalman filter.

1. Introduction

The heart is a vital organ that equals life for human beings as it beats constantly in the human body. Nevertheless, not only the functioning of this organ is complex but also its mechanism can be sometimes altered or even disrupted by different factors [1]. Moreover, the onset of heart disease can lead to death [2]. For this reason, establishing an adapted therapeutic strategy for a patient who suffers from heart disease is essential. This strategy requires several pieces of information about the patient's heart to evaluate the viability of the cardiac muscle through fixed or mobile systems [3]. In fact, many modalities are used to acquire images of the human heart. One of the least non-invasive modalities is magnetic resonance imaging MRI, a technique that allows the acquisition of functional (which enables locating the areas involved) and anatomical (which provides a realignment to correct a subject motion) images [4]. Cardiac MRI is used as a reference method that enables the detection of cardiac pathologies. The study of the different cardiac cavities, particularly the left and right ventricles, allows such detection. Figure 1 illustrates these cavities according to the short and long axis sections. The analysis and the quantitative assessment of the cardiac functions such as ejection fraction (EF) and myocardial mass (MM), as well as cardiac mass (CM), are frequently asked in clinical workflow [5]–[7]. In fact, MRI in cine mode is the most used acquisition in clinical routine because it allows continuous observation of cardiac kinetics. The MRI sequences performed provide both a 2D and 3D visualization. In addition, a view of 4D (3D+t) and 5D volume MRI sequences (flow sequences) can be realized [8]. This progress requires acquisition based on various slice planes. The main slice planes used for the right ventricle (RV) [9], which is the object of interest in this paper, are: the long axis 4 cavities slice and the short axis slice [10], [11].

In cardiac imaging, the segmentation of the contours of the ventricles is an essential step in detecting pathologies [12]–[14] such as ischemic, cardiomyopathies, and arrhythmias. Moreover, the monitoring of ventricular motion allows an in-depth analysis of these cardiovascular pathologies [15]. Although medical imaging provides essential support for the diagnosis of ventricle functions, their direct interpretation is still impeded by some constraints such as low resolution and the presence of strong noise that influence not only

the reliability of 2D segmentation but also the quality of 3D reconstruction. Thus, the use of spatio-temporal modeling techniques represents a notable alternative. This alternative follows three steps: the segmentation and modeling of ventricular contour and shape, the temporal monitoring of ventricular movement, and finally the analysis of computed parameters in the two previous steps for the establishment of the diagnosis.

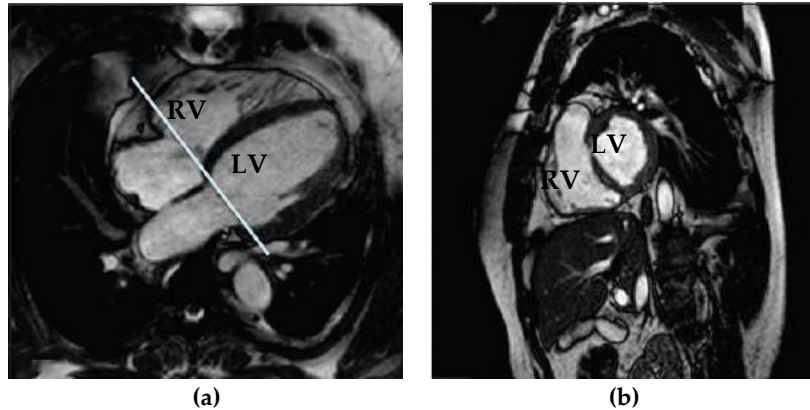


Figure 1. Cardiac MRI in diastolic phase (a) Long axis slice, (b) Short axis slice [10]

In this work, we will present a study of the right ventricle which is often underestimated [9],[16], and we will precisely focus on the first steps of the aforementioned process. In fact, the monitoring of the right ventricle motion is a key phase in the cardiac sequence analysis process that provides information about the temporal evolution of the RV. Nevertheless, monitoring either suffers from a lack of precision or causes high computing costs whenever the result is satisfactory. With regards to these issues, this work purports to introduce a generic monitoring method that is not only accurate but also adapted to the monitoring of periodic shapes such as the right ventricle. Throughout the whole cycle, full cardiac dynamics can be described which allows a direct interpretation of the RV functional parameters. The proposed approach is based on a Harmonic State Model (HSM) that provides first good modeling of a closed contour (a periodic evolution), and second an estimation of this contour which is made possible thanks to the model's robust state vector that helps to exploit the Kalman filter [17]. This function enables the use of the motion parameters such as velocity which represents a component of the model's state vector.

The model is linear and periodic, and it translates a dynamic model corresponding to the Fourier series decomposition [18] of cardiac movement. Used as a state model in a Kalman filter, this model provides a noise-resistant estimation of motion parameters such as speed and acceleration which are components of the state vector. So far, the Harmonic State Model has only been exploited in a temporal dimension to model the motion of the RV. The periodicity of the shape of the RV (closed surface) also allows us to transpose the model in a spatial dimension at a given time by introducing shape and smoothing constraints via harmonic decomposition. This double characteristic reveals the potential interest of such a model for 2D/3D tracking of the RV wall in a sequence of images.

This paper is organized as follows. Section 2 presents a brief state of the art of 2D segmentation, 3D reconstruction, and motion tracking methods. Section 3 then introduces the watershed segmentation method to enable endocardial and epicardial RV delineation. Section 4 deals with the volume reconstruction. In section 5, we outline the Linear Harmonic Model with the selected state equations which are to be followed by the estimation of motion parameters by Kalman filtering. In Section 6, the results are reported and succeeded by a discussion. Finally, Section 7 presents a brief conclusion and perspectives.

2. Related works

This section introduces a brief description of reference techniques in ventricular segmentation from cine MRI images as well as motion tracking of non-regular objects.

2.1. Cardiac cine MRI segmentation methods

The analysis of cine MRI sequences generally consists of three stages. First, a segmentation stage which includes segmentation of the wall in the successive images of the sequence. This stage is characterized by its difficulty as it is often performed in part manually because of the insufficient quality of the images. Second, a quantification stage of contraction or movement parameters by direct measurement or adapted modeling. Finally, an analysis stage which leads to the determination of the healthy or pathological character of the cardiac function under study. The work of several research groups gave rise to various publications concerning the analysis of marked MRI images [7], [19]–[21]. To contribute to a better understanding of these works, we will start with the concept of active contour [22] which was developed as a deformable curve in an attempt to get as close as possible to the contours of an image which helps locate and/or follow their movement over time. These active contours are used in many applications such as locating vessels in angiograms and tracking heart movement. Figure 2 showcases an example.

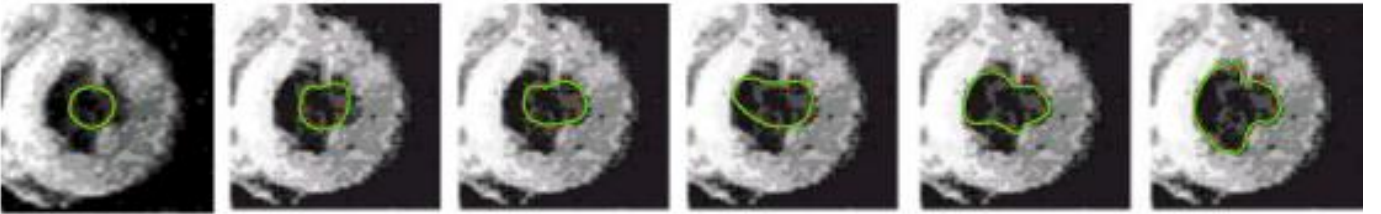


Figure 2. Left ventricle segmentation using active contours technique [23]

For a given deformable curve, the classical method initially defined by Kass et al. [23] is to associate certain energy at each position of the curve on the image. This energy is defined so that the ideal position of the curve (the contour to locate) corresponds to the minimum energy. The algorithmic complexity of the minimization processes leads to several iterations starting from an initialization already close to the result. The work of Amini et al. [24] was applied to a 2D time series of small-scale cuts with a grid-like marking pattern. The merit of this method is its low algorithmic complexity which is achieved thanks to the use of splines. Besides, the study was conducted only on interpolation points. However, follow-up problems appear for tags close to myocardial contours, mostly because of unreliable image energy. We recall that the myocardium represents the main muscle of the heart that ensures the emptying and filling of the cardiac cavities through the alternation between contractility and elasticity. The method developed by Young et al. [25] is a direct application of that of [23] to the entire grid with each line constituting a discrete snake. For each snake, the associated energy is defined as the sum of internal energy measuring elasticity and stiffness, image energy based on the intensity, and user energy, that allows manual intervention. The local weighting of these energies differs depending on whether or not they belong to the myocardium. This technique has the advantage of integrating regularity properties in the deformable grid which makes it more robust against noise. Contrarily to the method of Amini et al. [24], all the points of the grid move at the same time leading to the increase of the minimization algorithm's complexity. Radeva et al. [26] take into account all the superimposed slicing levels of a short-axis acquisition. Similar to Amini et al. work, slicing levels correspond to superimposed grids of tags a deformable 3D grid of splines, called B-solid and expressed as a 3D tensor product of B-splines. In fact, the search for the 3D matrix of the interpolation points is realized iteratively with minimal energy, yet in a significantly more complex way since the whole B-solid is deformed at the same time to converge towards the solution.

In this part we will deal with region-based segmentation, also called similarity-based segmentation which consists of converting an input image into a gray image to perform segmentation using morphological operations. The Watershed Algorithm [27]–[29] is indeed an important morphological technique. Based on this algorithm, the image is visualized on the topographic surface and the gray levels of a pixel are interpreted by its altitude. In fact, there exist several morphological techniques to perform image segmentation; however, the problem related to this segmentation is either condensed or overcome by the selection of the best marker-controlled algorithm. This marker can be applied directly to the gradient image in order to control segmentation [30]. In fact, many studies have been conducted on this subject to demonstrate the efficiency and powerfulness of the watershed algorithm in case of overlapping or rock formation [27]. An adapted algorithm that describes a parallel topological watershed transform inspired by Cousty et al. [32] original work is introduced in [31]. The recently published work of Kornilov et al. [33] presents an excellent description of open tools for watershed implementation. This algorithm remains a true source of inspiration and continues to operate successfully in image segmentation [34]–[38].

The aforementioned segmentation step can be followed by a volume reconstruction. In fact, while several studies have been proposed in the literature on the 3D reconstruction of the left ventricle, some researchers started to gain particular interest in the 3D modelization of the right ventricle given its importance to predict morbidity in patients with cardiac diseases. While an accurate assessment of the right ventricular function is crucial for the diagnosis of patients with pulmonary hypertension, the assessment of RV function is still challenging due to its complex morphology. Farooqi et al. [39] proposed a 3D model of the heart including the left and the right ventricles to aid surgeons in surgical planning. The model was generated from a 3D b-SSFP MRI sequence and the measurement results showed a good correlation compared to those generated from 3D echocardiography. Tautz et al. [40] proposed a 3D model of the right ventricle using 2D U-Net. Similarly, Küstner et al. [41] developed a new algorithm based on deep learning for 3D reconstruction of the right ventricle using cine MRI images. In their study, they proved that the proposed method allows rapid quantification of RV ejection fraction and offers acquisition of 3D cine MRI in less than 10 s. Furthermore, Dawes et al. [42] developed a 3D model of RV to predict pulmonary hypertension disease using supervised principal components analysis. The outcome of their study showed that the proposed 3D model improved the survival prediction of patients with cardiac diseases with an area under curve (AUC) of 0.73. Khoulood et al. [43] proposed an automatic watershed-based approach for left ventricular (LV) segmentation based on topology, geometry, and brightness priors before moving to 3D+t assessment in order to study the LV dynamics.

2.2. Tracking moving objects techniques

The processing of image sequences for tracking objects includes three points: detection, recognition, and tracking. Each point is characterized by different hypotheses and algorithmic tools.

The first step in image sequence processing is the detection of motion which indicates the possible existence of moving regions in the current image. These indicators then provide the basis for future algorithmic processing. There are indeed three types of methods characterized by the nature of the indicator they extract: the velocity-based approach [44], the primitive extraction approach [45], [46], and the regions of interest extraction approach [47], [48].

The next step is recognition. The goal is to obtain, at the end of this phase, a set of objects potentially usable for the dynamic aspects. It is a matter of refining or even decide the interest of particular areas of the image. We will organize the study of the different models of objects encountered along two axes: the appearance models and real models. Object appearance models are often used in cases where it is difficult to qualify the object because of excessive noise or in cases where objects are complex or diverse. In [48], the authors present the impossibility of defining an object model for their field of study as a justification for their approach. There is no object recognition but rather an area recognition. The models of real objects use characteristics of the object and they often exploit more natural properties. In [47], the object consists of a 3D polyhedron modeling a vehicle with twelve degrees of freedom. The set of contour segments obtained by the detection step is then matched with the edges of the polyhedral model by an iterative process introduced in [49]: minimize a criterion, defined by a measure of distance, for each edge of the polyhedron. In [50], the author uses a person model defined by a skeleton of six segments (two arms, two legs, torso, and head). In [51], a skeletal model of seventeen segments is used. A volume model consisting of fourteen elliptical cylinders is used in [52]. Time Matching and Tracking, contrarily to the previous steps whose treatments could be qualified as static, aimed at analyzing only one image. The methods which will be exposed in the continuation have an additional dimension to be treated: time. The purpose of processing in this step is to include the results of detection and recognition in the continuity of the image sequence. A first family of methods aims at matching these measurements with those obtained previously, while other techniques use these measurements to check the consistency of a prediction made thanks to all the results of the previous images. The first family of methods evoked by [53] is direct matching. The other popular family of tracking problem solving is Kalman filter estimation [17]. In this case, the treatment is done in two steps. First, a prediction of the current result is generated from the set of previous results, and then the predicted result is compared with the measurements obtained [46].

3. Proposed method for right ventricle segmentation

The right ventricular myocardium RVM is bordered by two contours: the epicardial (Ep) and the endocardial (En). We, therefore, consider: the right ventricular cavity RVC whose border is En and its complementary \overline{RVC} ; and the union of the RVC and the RVM , denoted $RVCM$, whose edge is Ep and its complementary is called ventricular fundus ($BV = \overline{RVCM}$).

3.1. Endocardial contour detection

The first step of RV segmentation consists of detecting the endocardial contour, thus primarily finding an RVC marker through the application of a threshold on the original image in order to separate the cavity from the rest. Then, this marker will be extended. A process of delimitation is applied by dilating the calculated marker at the level of pixels detected as potential candidates that may belong to the RVC . The results are shown in Figure 3.

3.2. Epicardial contour detection

In this section, we are interested in detecting the right ventricular epicardium based on the Watershed approach [54]. In order to guarantee an optimal implementation, a parallel version has been selected [31]. Based on the approach of Cousty et al. [32], the implemented version assures parallel watershed computing while preserving the given topology. In fact, prior minima extraction is not needed, and neither is the use of any sorting step or hierarchical queue.

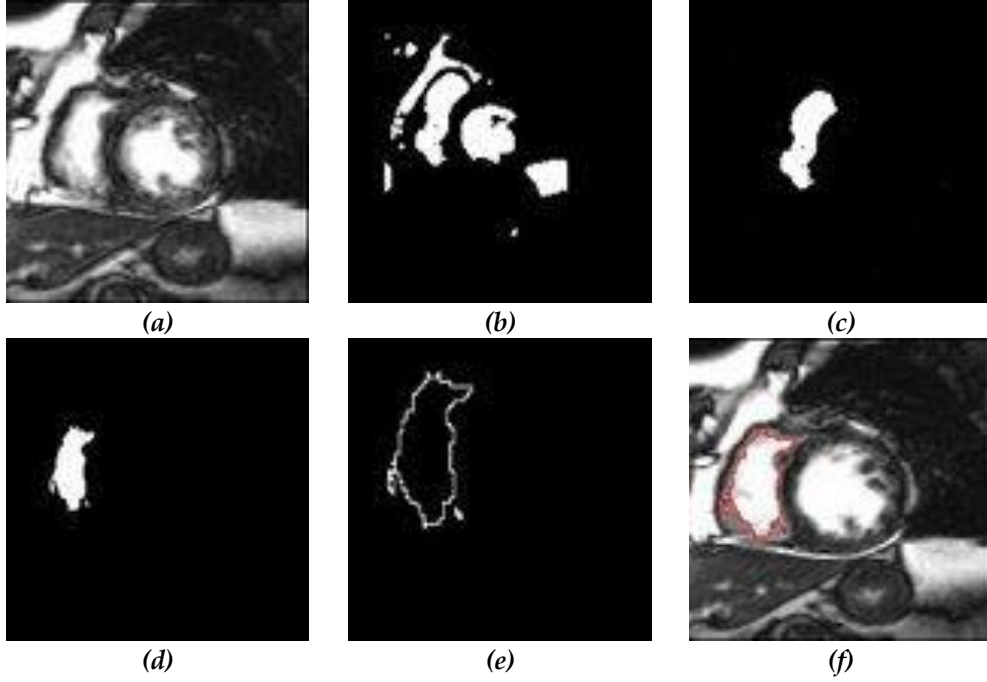


Figure 3. Endocardial border detection:(a) Original image in short axis view; (b) Result of the threshold; (c) Marker extraction; (d) RVC detection; (e) RVC border extraction; (f) Final result.

For this particular reason, we aimed at separating the ventricular background from the epicardial contour, which means the selection of two markers. To accomplish this, we relied on morphological and topological operators which enabled us to guarantee the respect of the a priori presented in the previous paragraph. The Ep border is then delimited from these markers and finally, a smoothing phase is performed:

- **RVMC Recognition:** This step is to determine the set of markers $RVMC_t$ for any $t \in [1, \text{sequence length}]$ for each image. It is a matter of dilating the RVC by making sure that the resulting set is included in the present RVMC.
- **BV Recognition:** The RVC thickness cannot exceed a certain threshold (s). We can deduce that the elements which are more distant from RVC_t than a distance equal to (s) must belong to the BV and therefore to the BV marker. The BV_t marker must be derived while preserving the topology by the homotopic transformations [55] which constitute a powerful tool. The BV has a single cavity: RVMC. The marker set $RVMC_t$ is, by construction, related. Moreover, it is necessarily included in the $RVMC_t$. The complement of this marker $\overline{RVMC_t}$ has then the desired topology for BV_t . Thus, marker BV_t can be derived from marker $RVMC_t$ by homotopic retraction. The idea is therefore to reduce the marker $\overline{RVMC_t}$ set while preserving its topology and respecting the constraints, using an ultimate homotopic constrained skeleton. A homotopic skeleton of a set R constrained by a set C has the same topology as R , contains C , and cannot be reduced (by point suppression) while preserving these two invariants. Therefore, we calculate the BV_t marker as the ultimate skeleton of $\overline{RVMC_t}$.
- **Delineation by Watershed transform:** To take the temporal coherence of the delineation process into consideration, we consider the 4D graph corresponding to the $3D+t$ image equation. The neighborhood of each voxel consists of its 6 neighbors in 3D space. The voxel that precedes it and the one that follows it in the temporal equation. Each edge of this graph is valued by the difference in intensity of the two voxels that compose it. The Watershed is calculated on the edges of this 4D graph from the

markers corresponding to the union of the marker RVMct and the marker BVt in time. It can be noticed that the evaluation of the edges connecting two voxels belonging to a temporal gradient corresponds to two successive images. Considering this temporal component enables us to maintain a generic coherence between the successive segmentations during the cardiac cycle, which leads to an epicardium segmentation.

- **Smoothing:** In order to smooth the epicardial border and restore a satisfactory shape in places where the contrast information does not allow a correct Watershed delineation, we use the Alternating Sequential Filter (ASF) [56], [57]. The ASF is a sequence of openings and closings by balls of increasing size. It is important to emphasize the effectiveness of the parallel version presented in [58]. The results are shown in Figure 4.

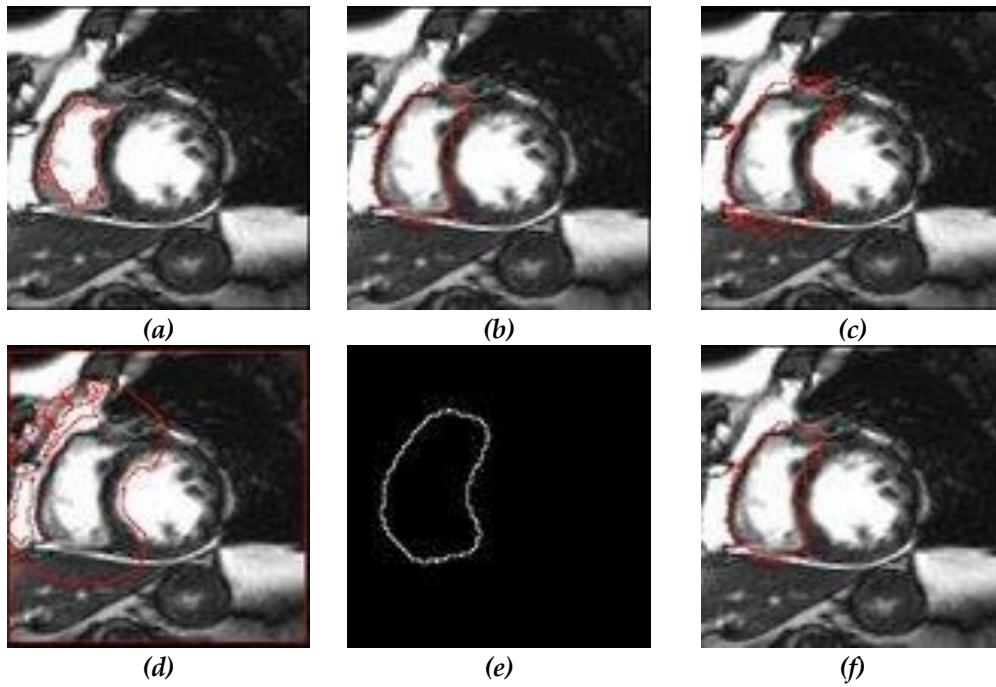


Figure 4. Epicardial border detection:(a) RVC border already detected; (b) Selection of Ep marker; (c) Selection of BV marker; (d) Delineation by Watershed transform; (e) Extraction of Ep border; (f) Final result.

3.3. Myocardium extraction

The final step is to join the two output images of the epicardium and endocardium border detection to find the myocardium automatically as shown in Figure 5.

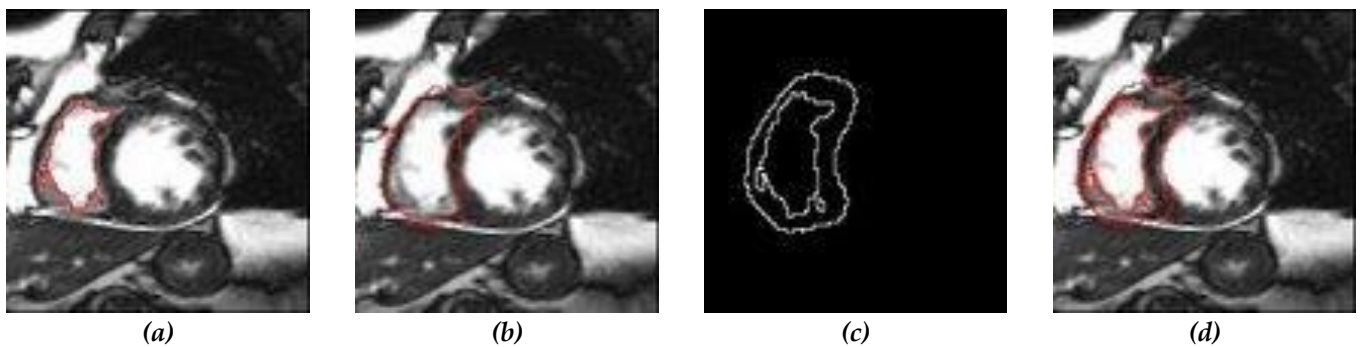


Figure 5. Myocardial border detection: (a) En border detection result; (b) Ep border detection result; (c) Myocarditis border extraction; (d) Myocardial border detection result after detection of the En and Ep borders.

We aim to evaluate the semi-automatic image segmentation short-axis cardiac MR method, which segments all RV contours in one cardiac phase with minimal user input and without any manual corrections (Figure 6). The validity of the semi-automatic segmentation is compared to manual segmentation.

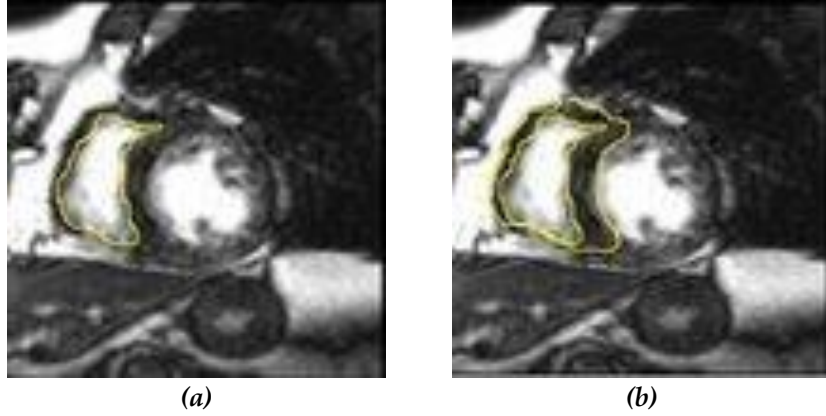


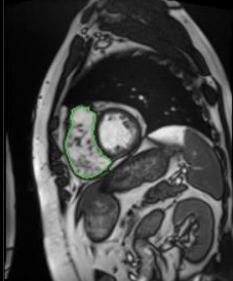
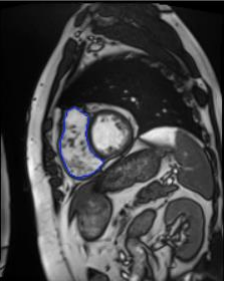
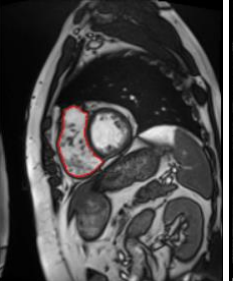
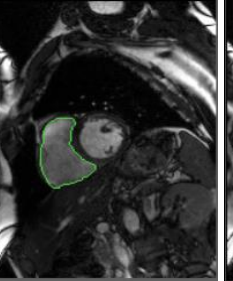
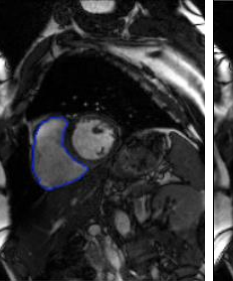
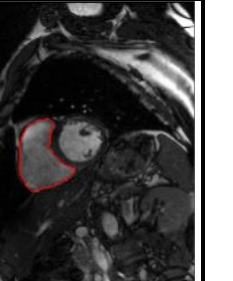
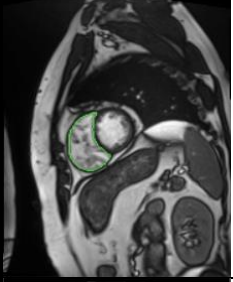
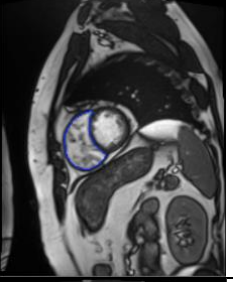
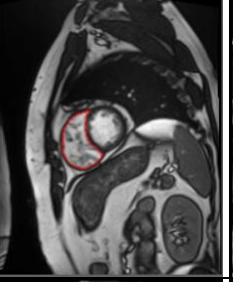
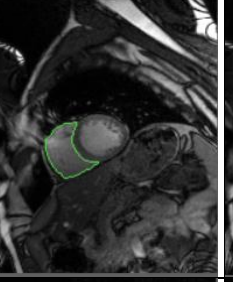
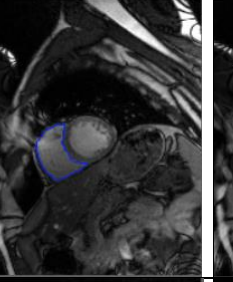
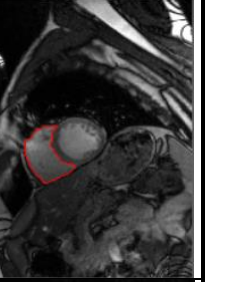
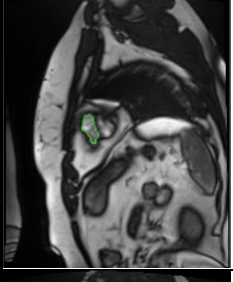
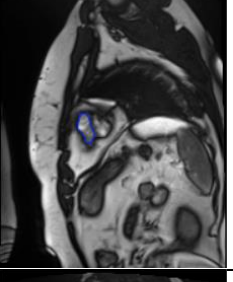
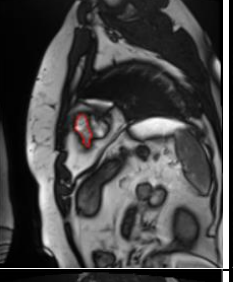
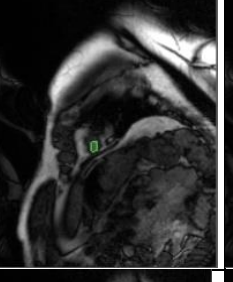
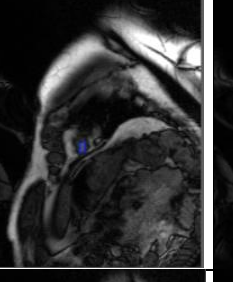
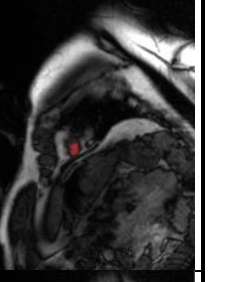

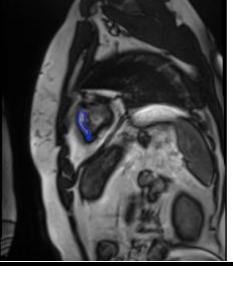
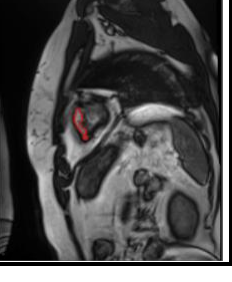
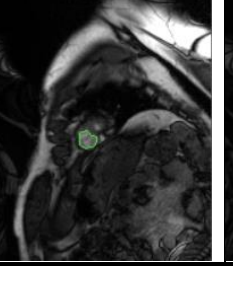
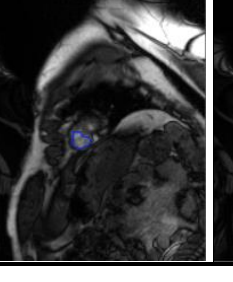
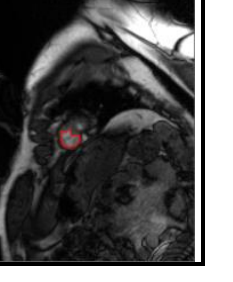
Figure 6. RV manual segmentation in yellow: (a) endocardial detection, (b) myocardial extraction.

It was revealed that manual segmentation is time-consuming because it depends on various factors such as user experience and contour detection methods. The main difficulty lies in the uniform delineation of the endocardial wall. If short-axis slices are used, delineation of the basal slices becomes extremely delicate. On the other hand, if strictly axial slices are used, the inferior wall of the right ventricle rises and becomes practically impossible to delineate [59], [60]. To summarize, the robustness of right ventricular measurements raises many questions. The postprocessing time as well as the variability of the measurements are twice as high as the analysis of the left ventricle. Conditioned by expert experience (see table 1) and appropriate slices selection, the variations of inter-observer and intra-observer coefficients are 10% and 13%, respectively. It is important to note that these two coefficients do not exceed 5% and 8% when analyzing the LV [61].

Table 1. Manual vs automated segmentation results. First and second columns: expert 1 and expert 2 annotations of different slices of patient1 respectively

	PM vs. exp1	PM vs. exp2	Exp1 vs. exp2
<i>End-systolic-time</i>			
Sensitivity	0.95	0.99	0.98
Specificity	0.99	0.99	0.99
Dice	0.96	0.93	0.93
Precision	0.97	0.89	0.89
Recall	0.95	0.99	0.98
<i>End-diastolic-time</i>			
Sensitivity	0.96	0.95	0.95
Specificity	0.99	0.99	0.99
Dice	0.97	0.95	0.97
Precision	0.98	0.95	0.99
Recall	0.96	0.95	0.95

Table 2 Manual vs automated segmentation results. First and second columns: expert 1 and expert 2 annotations of different slices of patient 1 respectively. Fourth and fifth columns: expert 1 and expert 2 annotations of different slices of patient 2 respectively. Third and sixth columns: our proposed method segmentation results of patient 1 and patient 2 respectively.

Patient 1			Patient 2		
Expert 1 - Manuel	Expert 2 – Manuel	Proposed method	Expert 1 - Manuel	Expert 2 – Manuel	Proposed method
					
					
					
					

In fact, inter-expert variability has a major influence in interpreting the segmentation quality results as shown in Ammari et al. work's [62]. For this reason, we wanted to compare our algorithm's output with two different manual segmentation held by two expert radiologists from Fattouma Bourguiba hospital. Table 2 illustrates the manual segmentation of the two experts showing similarities in some slices and few differences found within others. Contrarily, the results returned by our method are homogeneous, and stable without any variability except the inter-patient one. Semi-automatic segmentation methods which assist the analyst in this process in a short period of time and which provide valid results will be very beneficial to the physician in their clinical work. Our segmentation method provides, indeed, promising results as it takes less segmentation time.

4. Volume reconstruction

Volumetric reconstruction of the right ventricle is an excellent way to guarantee a better visualization of the result of the previous segmentation. To achieve this, we first generate meshes from the obtained sequences, see figure 7, before proceeding to smoothing. Figures 8 and 10 show respectively the reconstructions of volumes from two different patients at the End-Diastolic phase and the End-Systolic phase after computing volume parameters that confirm pathological cases (Patient 1 – a 37-year-old man with inferior infarction extended to the VD) as shown in table 3. It should be noted that patient 2 who is a 49-year-old man is healthy. Volume rendering and computing are obtained using Amira software. For a more refined result, 3D slicer was used to obtain smoother contours and separation of the endo and epicardial cavities as shown in figures 9 and 11.

Table 3. Volume (mm³) results of the two patients' RV constructions.

Patient 1		Patient 2	
VTD	VTs	VTD	VTs
143700.9	103800.2	84000.1	37000.4

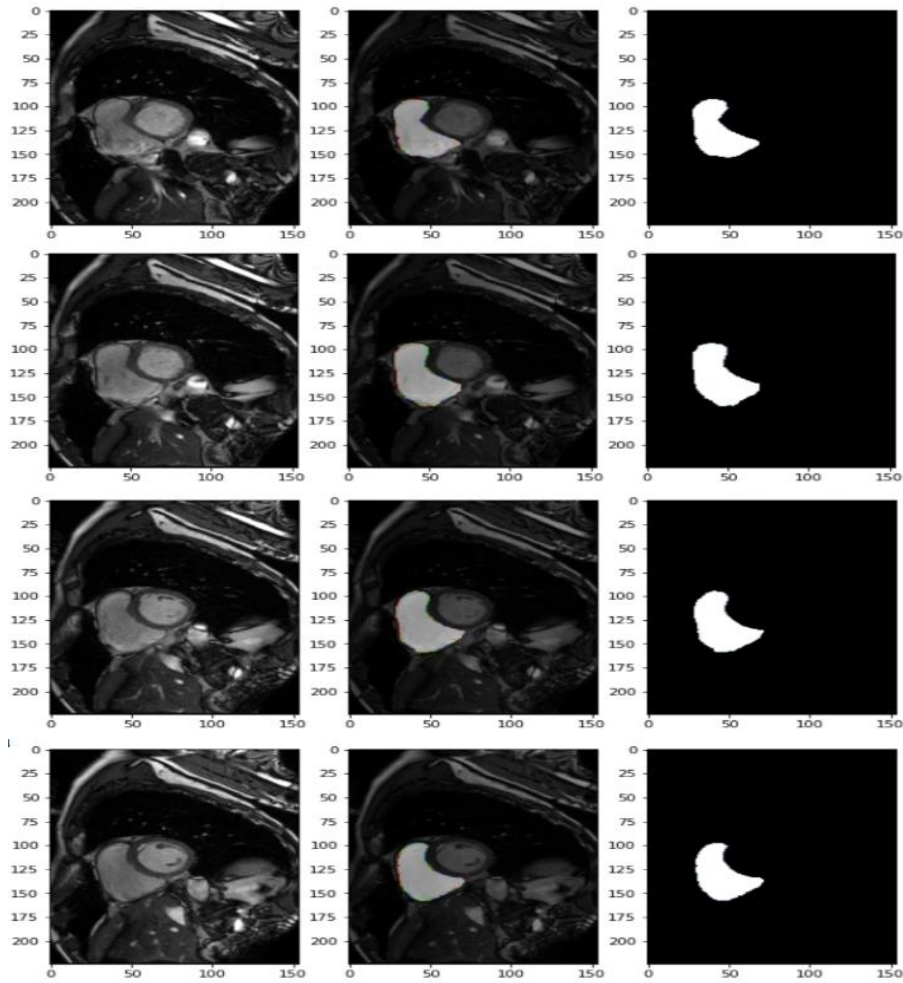
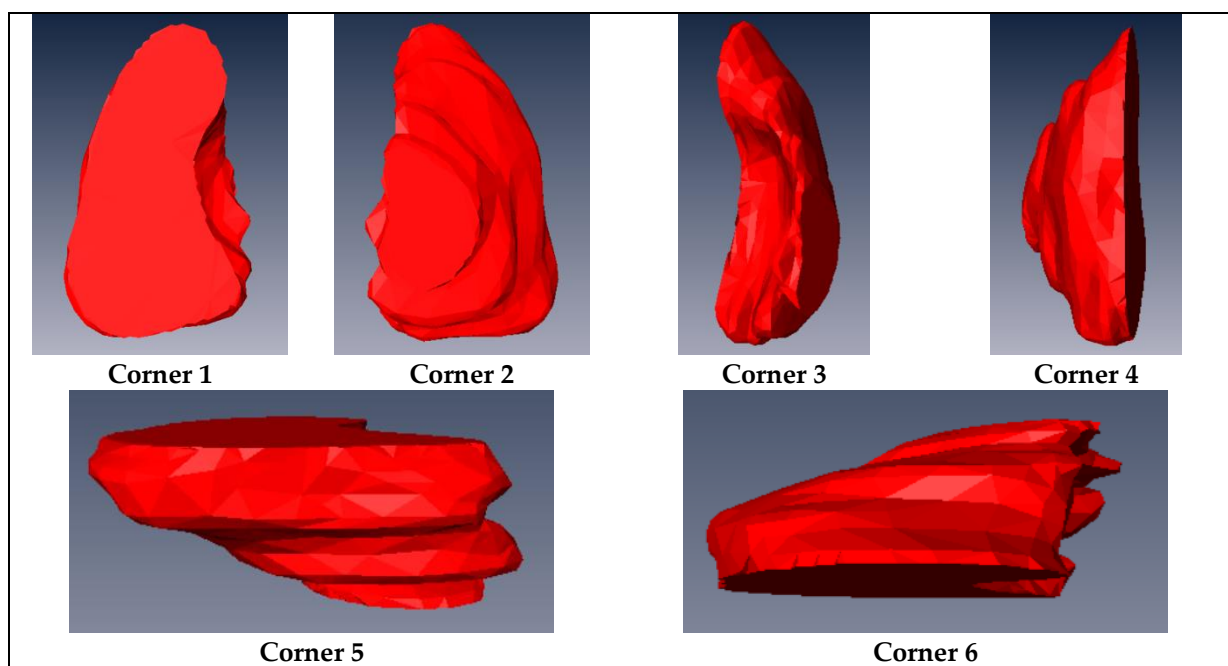
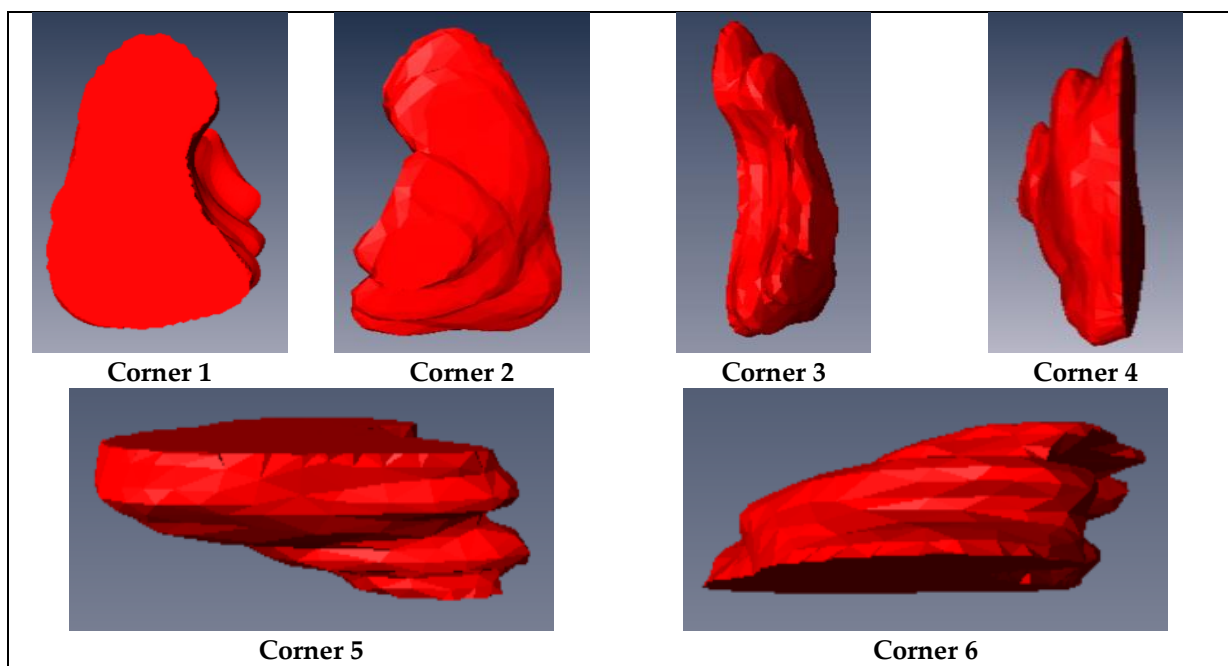


Figure 7. The final result of RV segmentation. The first row displays the original MRI slices; The second row displays the superposition of the extracted mask with the original image; The third row displays the extracted contours.



(a)



(b)

Figure 8. 3D volume of Patient 1's RV demonstrated using AMIRA software: (a) at the End-Diastolic phase, (b) at the End-Systolic phase using AMIRA software.

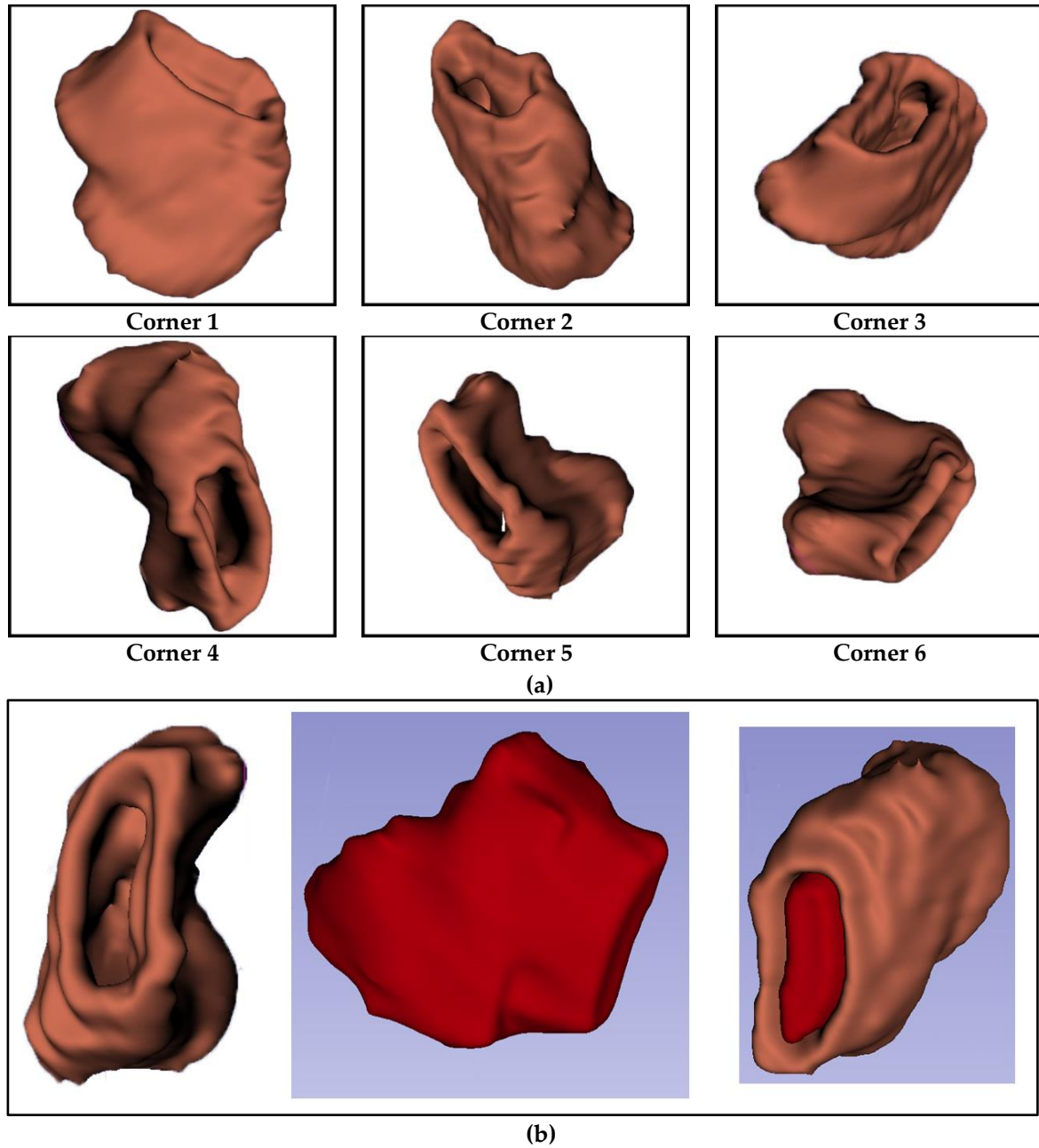
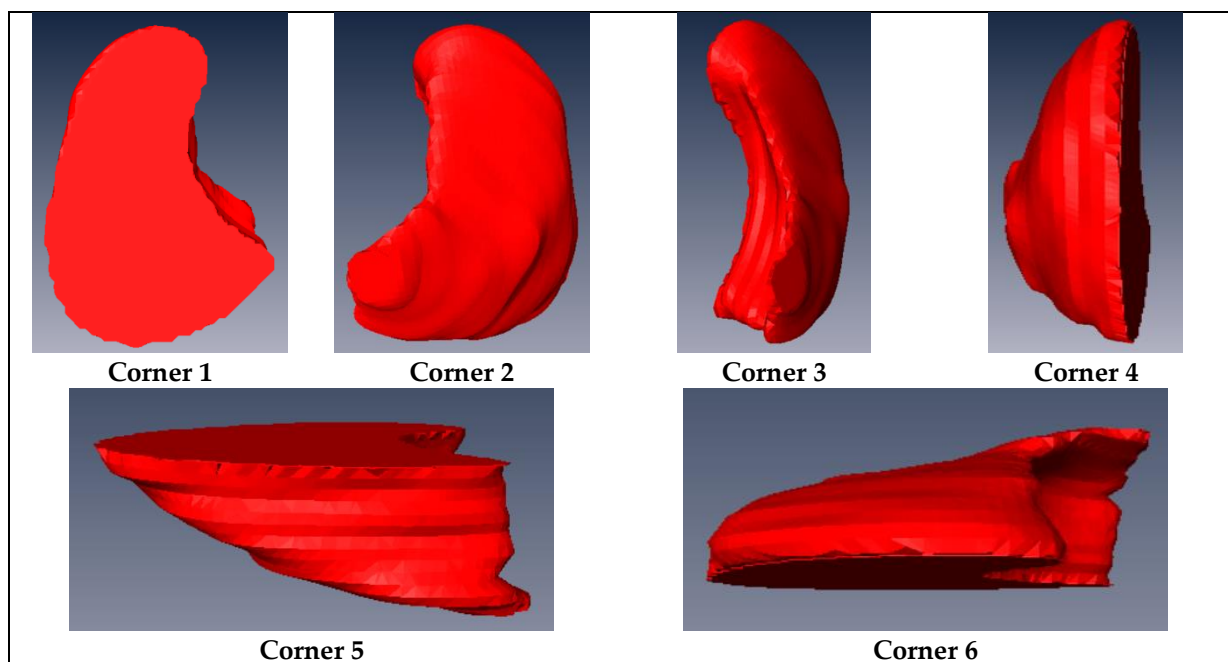
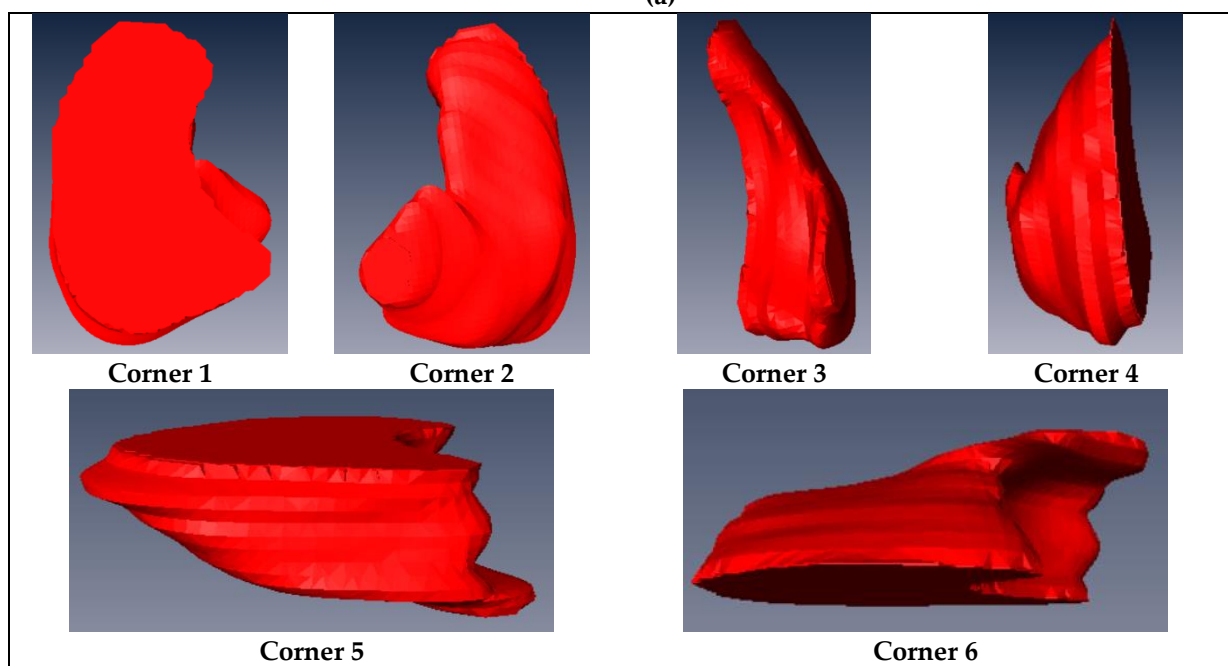


Figure 09. 3D volume of Patient 1's RV demonstrated using 3D slicer Software: (a) Different corner views (b) Full reconstruction of Endo and Epicardial volumes.



(a)



(b)

Figure 10. 3D volume of Patient 2's RV demonstrated using AMIRA software: (a) at the End-Diastolic phase,(b) at the End-Systolic phase.

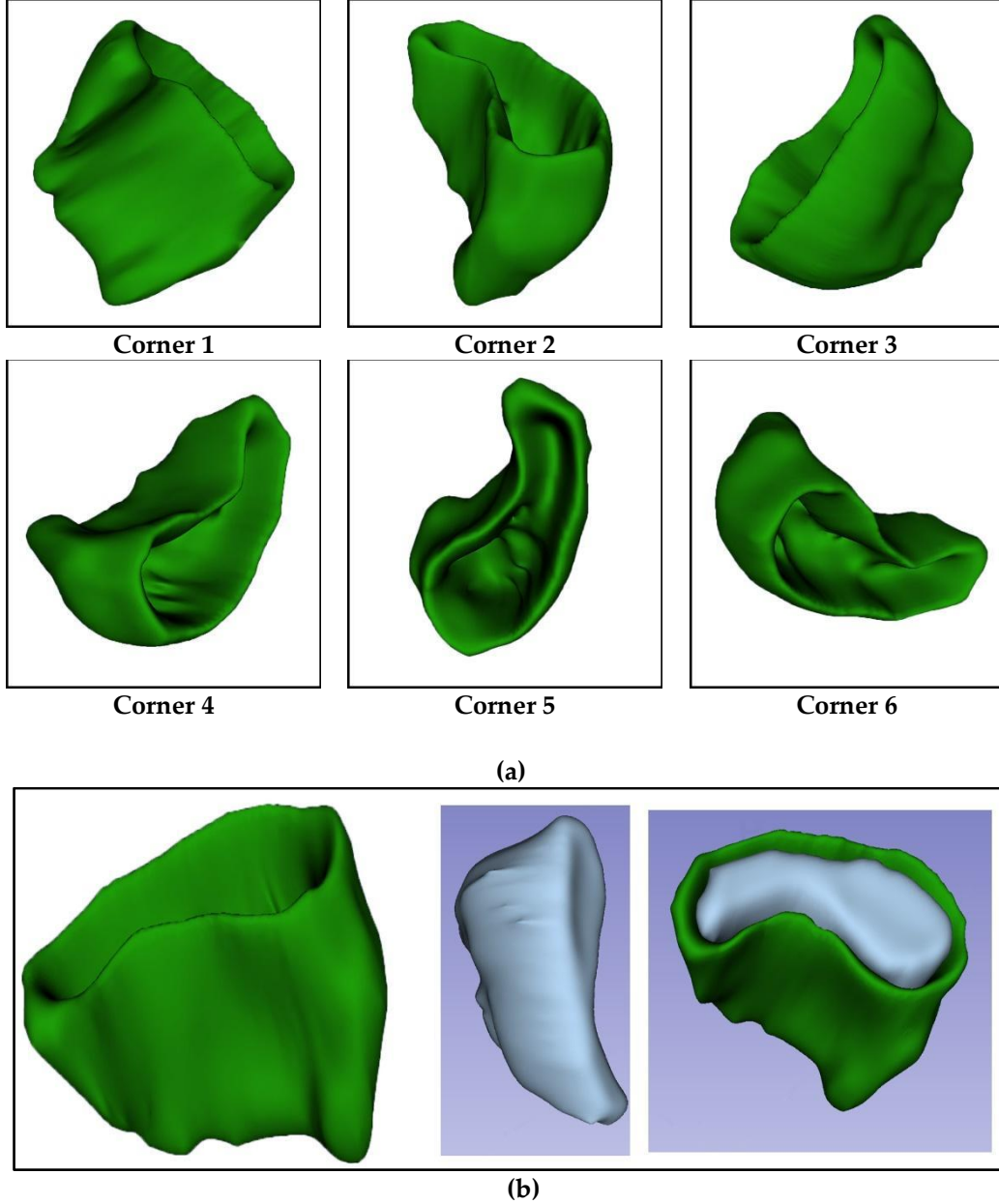


Figure 11. 3D volume of Patient 2's RV demonstrated using 3D slicer Software. (a) Different corner views (b) Full reconstruction of Endo and Epicardial volumes

5. Modeling the cardiac right ventricle motion

In this section, we are interested in modeling the right ventricle (RV) motion for analysis. We propose to model the spatio-temporal trajectory of the points belonging to the endocardial (respectively epicardial) contour of the RV using a harmonic linear motion model that can describe the RV dynamics. This model is based on the hypothesis of the quasi-periodicity of the heart rhythm. It uses a Kalman filter as an estimation tool. It is inspired and strongly guided by Oumsis et al. [63] approach initially introduced for LV motion tracking. The descriptor models of the cardiac function can be classified into two large families.

The *harmonic decomposition in Fourier series* of the cardiac movement [64], [65] is based on the hypothesis of quasi-periodicity of the cardiac rhythm of which a descriptor $s(t)$ can be decomposed into a Fourier series as shown in equation (1). In fact, $s(t)$ represents an attribute extracted from the sequence of images, which may be local like the

coordinates of a point on the wall of the RV, or more global like the main radius or axes of the RV. \bar{s} represents its average value. This model of movement, known as the harmonic model, is therefore in the form of a harmonic series of order n . The coefficient ω represents the pulsation while $\phi(i)$ represents the phases of the different harmonics of the model.

$$S_n(t) = \bar{s} + A_{(1)}\sin(\omega t + \phi_{(1)}) + \dots + A_{(n)}\sin(n\omega t + \phi_{(n)}) \quad (1)$$

The *State vector linear dynamic modeling* methods provide a complete description of the motion of the system under study [42], [45]-[47]. In continuous time, system evolution is governed by a linear differential equation. In discrete time, the state of the system at the instant $k+1$ is given by equation (2); where k is the time variable, F is the transition matrix allowing the shift of the state vector $S(k)$ from one instant to another; a Gaussian noise $\zeta(k)$ with a zero mean of covariance matrix $Q(k)$.

$$S(k+1) = F \cdot S(k) + \zeta(k) \quad (2)$$

The two previously mentioned motion models are solely temporal (1D) models, independent of any geometric representation of the RV. They can be merged with a 2D or 3D spatial model that models the shape of the RV to provide spatiotemporal models.

Assuming that the motion of the right ventricle is quasi-periodic, we consider $s(t)$ as an attribute of the ventricle extracted from a temporal sequence of heart images. The attribute can be for example the coordinates of a point having a value that evolves during the cycle in a periodic way. We will consider it as a signal which can be decomposed according to equation (1) in the Fourier domain into a sum of harmonics. The objective is to have a linear state model without limiting the number of harmonics using equation (2) which corresponds to the harmonic decomposition of equation (1).

5.1 State vector characterization

For the sample k corresponding to time t , the motion of the RV as described in equation (1) will be characterized as follows:

$$s_{(n)}(k) = s_{(n)}(t) = \bar{s} + A_{(1)}\sin(\omega t + \phi_{(1)}) + \dots + A_{(n)}\sin(n\omega t + \phi_{(n)}) \quad (3)$$

The sample $k+1$ corresponds to the time $t+\Delta t$; it will be characterized as follows:

$$\begin{aligned} s_{(n)}(k+1) &= s_{(n)}(t+\Delta t) = \bar{s} + A_{(1)}\sin(\omega(t+\Delta t) + \phi_{(1)}) + \dots + A_{(n)}\sin(n\omega(t+\Delta t) + \phi_{(n)}) \\ s_{(n)}(t+\delta t) &= \bar{s} + A_{(1)}\sin(\omega t + \phi_{(1)})\cos(\omega\Delta t) + \dots + A_{(n)}\cos(n\omega t + \phi_{(n)})\sin(n\omega\delta t) \end{aligned} \quad (4)$$

In equation (3), $s_{(n)}(t)$ is a linear combination of the terms $A_{(i)}\sin(i\omega t + \phi_{(i)})$. In equation (4), $s_{(n)}(t+\Delta t)$ is also expressed by a linear combination of the same $A_{(i)}\sin(i\omega t + \phi_{(i)})$ and $A_{(i)}\cos(i\omega t + \phi_{(i)})$.

The objective here is to find a state vector $S_{(n)}$ that contains the element $s_{(n)}$ and allows $s_{(n)}(t+\Delta t)$ computing according to $s_{(n)}(t)$. Considering $s_{(n)}^{(i)}(t)$ the derivative of $s_{(n)}(t)$ in order i with respect to t , the following equations system is then extracted:

$$\begin{cases} s_n(t) = \bar{s} + A_1 \sin(\omega t + \phi_1) + \dots + A_n \sin(n\omega t + \phi_n) \\ s_{(n)}^{(2)}(t) = -\omega^2 A_1 \sin(\omega t + \phi_1) - \dots - (n\omega)^2 A_n \sin(n\omega t + \phi_n) \\ s_{(n)}^{(2(n-1))}(t) = (-1)^{n-1} \omega^{2(n-1)} A_1 \sin(\omega t + \phi_1) + \dots + (-1)^{n-1} (n\omega)^{2(n-1)} A_n \sin(n\omega t + \phi_n) \end{cases} \quad (5)$$

This linear system of n equations has n unknowns represented by **equation (6)**:

$$V_{(n)}(t) = (A_{(1)} \sin(\omega t + \phi_{(1)}), \dots, A_{(n)} \sin(n\omega t + \phi_{(n)}))^T \quad (6)$$

The resolution of **system (5)** allows to write each element of the vector $V_{(n)}(t)$ as a linear combination of the elements of the vector $(\bar{s}, s_{(n)}(t), s_{(n)}^{(2)}(t), s_{(n)}^{(4)}(t), \dots, s_{(n)}^{(2(n-1))}(t))^T$ of dimension $n+1$. Let be \bar{r}_i and $r_{(ij)}$ ($i=1, \dots, n; j=0, \dots, n-1$) the coefficients of this combination:

$$A_{(i)} \sin(i\omega t + \phi_{(i)}) = \bar{r}_i \bar{s} + \sum_{j=0}^{n-1} r_{(i,j)} s_{(n)}^{(2j)}(t) \quad (7)$$

So by derivation, we obtain:

$$A_{(i)} \cos(i\omega t + \phi_{(i)}) = \frac{\sum_{j=0}^{n-1} r_{(i,j)} s_{(n)}^{(2j+1)}(t)}{i\omega} \quad (8)$$

According to $A_{(i)} \sin(i\omega t + \phi_{(i)})$ and $A_{(i)} \cos(i\omega t + \phi_{(i)})$ previously defined; we can express $s_{(n)}(t + \Delta t)$ using the following vector $S_{(n)}(t) = (\bar{s}, s_{(n)}(t), s_{(n)}^{(1)}(t), s_{(n)}^{(2)}(t), \dots, s_{(n)}^{(2(n-1))}(t), s_{(n)}^{(2n-1)}(t))^T$ of dimension $2n+1$.

Thus, the vector $S_{(n)}(t)$ of dimension $2n+1$ can be chosen as the state vector of the harmonic state model: $S_{(n)}(t) = (\bar{s}, s_{(n)}(t), \dots, s_{(n)}^{(2n-1)}(t))^T$ (9)

5.2 Transition matrix computing

The evolution equation of the harmonic equation model will be described as follows

$$S_{(n)}(t + \Delta t) = F_{(n)} S_{(n)}(t) + \zeta(t)$$

The transition matrix $F_{(n)}$ can be directly computed by solving **system (5)**. This system expresses the vector $V_{(n)}(t)$ as a function of the vector $S_{(n)}(t)$ which allows for determining the matrix elements. The transition matrix can also be determined recursively from the transition matrix of the harmonic model of order $n-1$ following **equation (10)** that expresses the second line of the matrix $F_{(n+1)}$. As explained by Ousmis et al. [63], the expressions $s_{n+1}^i(t + \Delta t)$ are calculated by deriving this expression with respect to (Δt) . The state model thus obtained [63] is a canonical model that has the advantage of providing the successive derivatives of the observed parameter as its state vector.

$$\begin{aligned} s_{(n+1)}(t + \Delta t) = & \left[\bar{a}_1 - \bar{r} \sum_{j=0}^{n-1} (-1)^j a_{1,2j} ((n+1)\omega)^{2j} + \bar{r} \cos((n+1)\omega\Delta t) \right] \bar{s} \\ & + \sum_{i=0}^{n-1} \left[a_{1,2i} - r_i \sum_{j=0}^{n-1} (-1)^j a_{1,2j} ((n+1)\omega)^{2j} + r_i \cos((n+1)\omega\Delta t) \right] s_{n+1}^{2i} \\ & + \sum_{i=0}^{n-1} \left[a_{1,2i+1} - r_i \sum_{j=0}^{n-1} (-1)^{j+1} a_{1,2j+1} ((n+1)\omega)^{2j+1} + r_i \frac{\sin((n+1)\omega\Delta t)}{(n+1)\omega} \right] s_{n+1}^{2i+1} \\ & + \left[-r_n \sum_{j=0}^{n-1} (-1)^j a_{1,2j} ((n+1)\omega)^{2j} + r_n \cos((n+1)\omega\Delta t) \right] s_{n+1}^{2n}(t) \\ & + \left[-r_n \sum_{j=0}^{n-1} (-1)^{j+1} a_{1,2j+1} ((n+1)\omega)^{2j+1} + r_n \frac{\sin((n+1)\omega\Delta t)}{(n+1)\omega} \right] s_{n+1}^{2n+1}(t) \end{aligned} \quad (10)$$

5.3 Recursive filter building:

In this subsection, a Kalman filter is defined from the computed harmonic state model to overcome the noisy measurements obtained from cardiac image sequences. The Kalman filter-based process can be divided into two stages: The first step consists in predicting the estimation according to the model of the system. To achieve this, the Kalman filter takes the previous estimate of the parameters with eventual errors and predicts the new parameters according to the modeling of the system. The second step will update this prediction by virtue of the new measurements. In fact, this update step will rectify any errors that would exist in the model.

The complete state model of a linear system consists of the state equation (2) and the measurement equation that relates the state vector to the measured quantities. In the present case, the only variable $S(k)$ with $H(0,1,0,\dots,0)$ and $\zeta(k)$ is a zero mean additive Gaussian noise of a covariance matrix of $Q(k)$. $s_z(k)$ is the measurement vector that groups together the observations made on the system at time k , which is reduced to the measurement of the attribute $s(k)$. It is linked to the state vector by the measurement equation H . $\eta(k)$ is a zero mean Gaussian noise of covariance matrix $R(k)$.

$$\begin{aligned} S(k+1) &= FS(k) + \zeta(k) \\ S_z(k) &= HS(k) + \eta(k) \end{aligned} \quad (11)$$

The use of such a filter allows the estimation of the state vector to converge towards optimal estimates of the parameters of the dynamic system. Thus, after convergence over a sufficient number of periods, the information contained in the state vector will allow describing the evolution of this parameter. It is important to note that the matrix $R(k)$ was reduced to a matrix (1×1) of a single element. $Q(k)$ is chosen as a diagonal matrix $(2n+1) \times (2n+1)$. The values of this diagonal represent the noise present in the system.

6. Results and Discussion

To evaluate the proposed approach, an intern database of twenty patients was used. These data, made anonymous, come from classical clinical exams performed at Fattouma Bourguiba University Hospital, Monastir, Tunisia. They concern both healthy volunteers as well as pathological cases. Moreover, they were collected following the Declaration of Helsinki, and the protocol was approved by the Ethics Committee of Laboratory of Medical Imaging Technology - LTIM-LR12ES06, Faculty of Medicine of Monastir Tunisia, (December 15, 2021). Before taking part in this study, all volunteers gave their informed consent for inclusion.

The simulation of the motion was initially developed using a third-order harmonic equation (13). \bar{s} , $A_{(1)}$, $A_{(2)}$, $A_{(3)}$, $\varphi_{(1)}$, $\varphi_{(2)}$, $\varphi_{(3)}$, ω are set out in **Table 4**.

$$s(t) = \bar{s} + A_{(1)} \sin(\omega t + \varphi_{(1)}) + A_{(2)} \sin(2\omega t + \varphi_{(2)}) + A_{(3)} \sin(3\omega t + \varphi_{(3)}) \quad (13)$$

The same test conditions announced in [63] are maintained: The measurement of noise is simulated by adding a white Gaussian noise of mean zero and variance σ^2 . The number of samples is fixed at 16. This data is fed to the Kalman filter which estimates the state vector $S_{(n)}(t)$ of the harmonic state model.

TABLE.4- Fixed Data for Kalman estimation

\underline{s}	A_1	A_2	A_3	φ_1	φ_2	φ_3	$\omega/2\pi$
4.50	13.06	-0.64	4.33	-1.37	1.66	0.65	100/60

These data are used in the Kalman filter which estimates the state vector $S_{(n)}(t)$ of the harmonic state model. **Figure 12** illustrates the behavior of the filter from any initialization to convergence. After a learning period of two cycles, the Kalman filter converges towards optimal estimates of dynamic system parameters. Thus, the information contained in the state vector will enable the description of the evolution of this parameter. However, this experience was a preliminary result that established the feasibility of the approach and required the implementation of a broader strategy to evaluate and clinically validate the method.

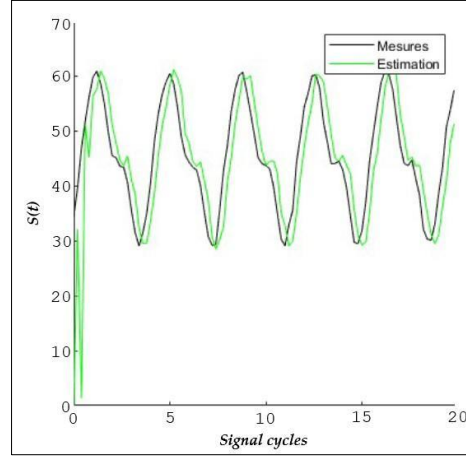


Figure 12. Behavior of the filter built from the 3rd order model.

Two estimation errors are calculated and for each filter [63]: the mean square error ϵ_1 between the filter estimate and the exact signal values (without noise), and the mean square error ϵ_2 between the filter estimate and the noisy measurements as shown by the following equations.

$$\epsilon_1 = \sqrt{\frac{1}{N} \sum_{k=1}^N \left\| \hat{s}_k^k - s(k) \right\|^2}$$

$$\epsilon_2 = \sqrt{\frac{1}{N} \sum_{k=1}^N \left\| \hat{s}_k^k - sz(k) \right\|^2}$$

We notice that the model of order 3 ensures the smallest error ϵ_1 , which is indeed a logical result. The order of the state model corresponds to the number of harmonics of the signal. Error ϵ_1 is impossible to calculate in practice; as a result, it impedes us from choosing this order. Error ϵ_2 decreases as the order of the harmonic state model increases so that the high-frequency components of the noise can be taken into account. **Figure 13** shows the evolution of the two errors ϵ_1 and ϵ_2 as a function of the order of the harmonic model.

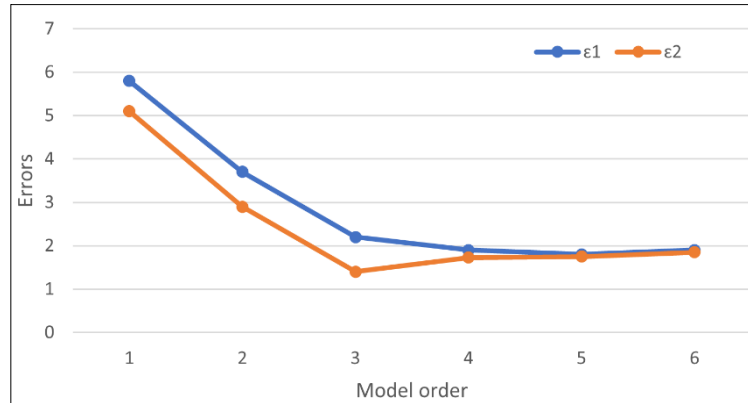


Figure 13 Evolution of the errors ϵ_1 and ϵ_2 according to the model's order.

For a faithful application of cardiac motion, a system with sufficient harmonics to model motion should be chosen. The study of the average value of the amplitude of each harmonic of the signals formed by the variation of the state model over time will allow making such a choice. In **Figure 14**, the mean value of the amplitudes of the first six harmonics is plotted. It can be noticed that the first three harmonics are sufficient to model the temporal variations of the external and internal rays as well as thickening. A model of order 3 is therefore used.

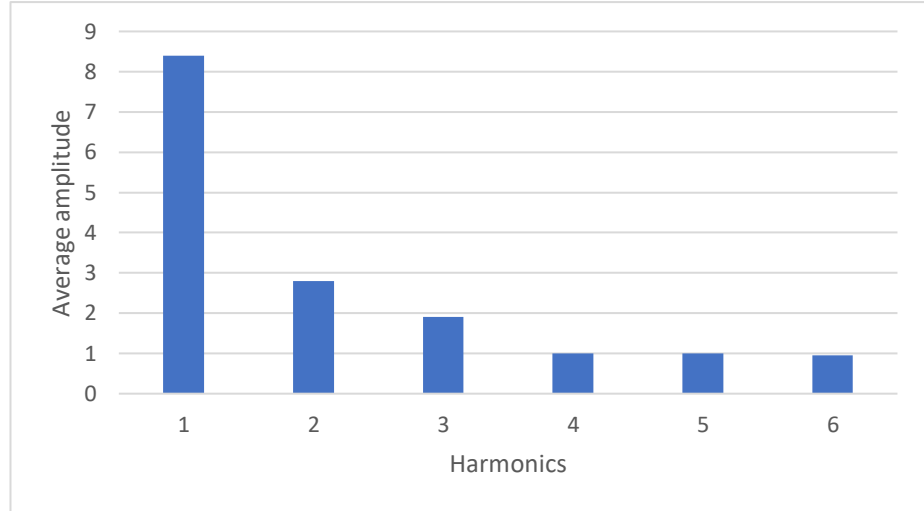


Figure 14 Mean amplitude of signal harmonics

Finally, measuring the distance involves superimposing the two contours of the endocardium and the epicardium. This process is iterated until the last image (this sequence contains 14 images). Then, the Euclidean distance between each pair of corresponding points is calculated (**Figure 15**); and this is for each direction, by determining the intersection points of two lines.

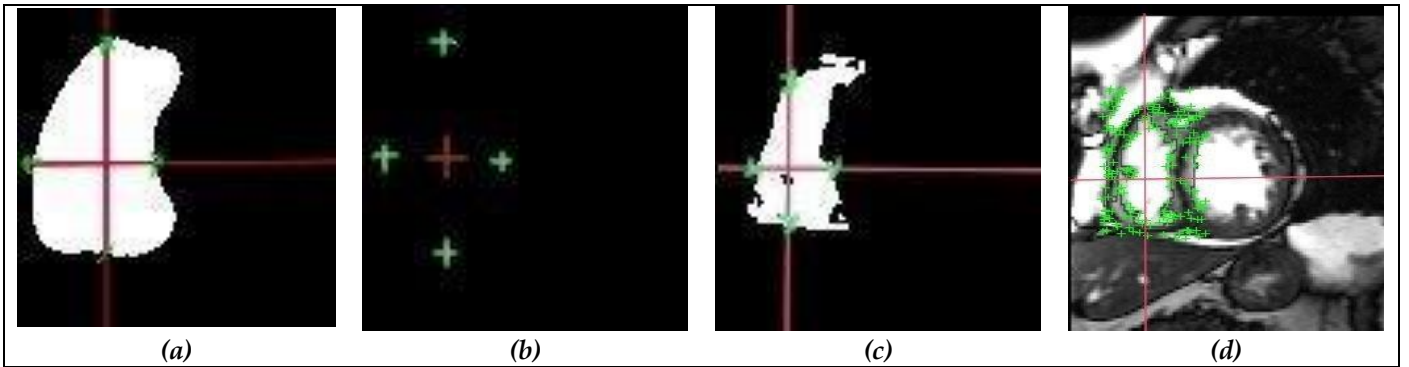
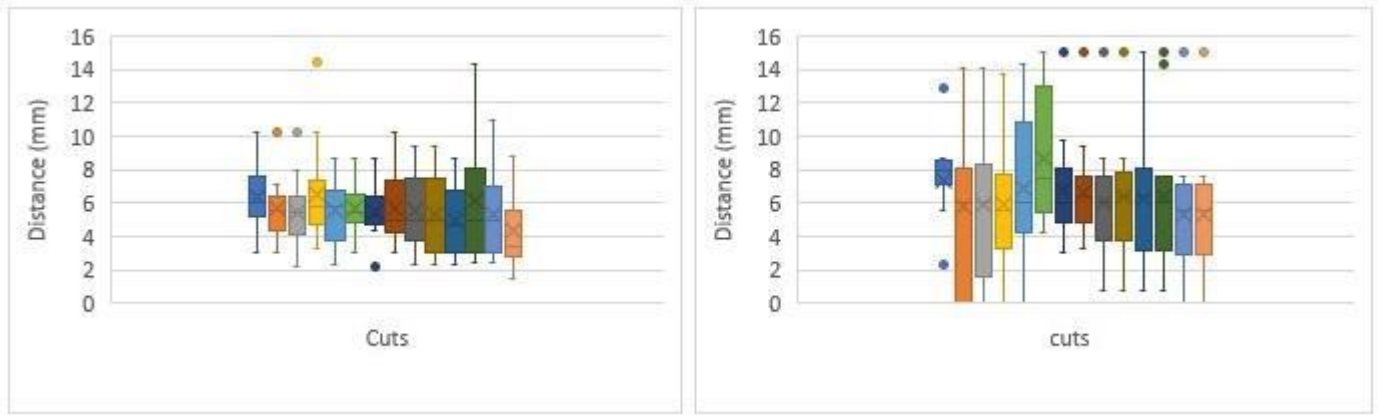


Figure 15. (a) Intersection of the segmented image with endocardium, (b) Intersection of the lines with the contour of the endocardium, (c) Intersection of the segmented image with epicardium, (d) Four myocardial distances.

We note that the thickness of the walls in the normal case is between 2 to 5mm; when this value is above 6mm, it is a pathological case. **Figures 16** illustrate results for diastole and systole phases. The evolution of the average distances between the different cuts is presented in **Figure 17** for both systole (S) and diastole (D) phases.



(a)

(b)

Figure 16. Distance computing for (a) diastolic and (b) systolic phases.

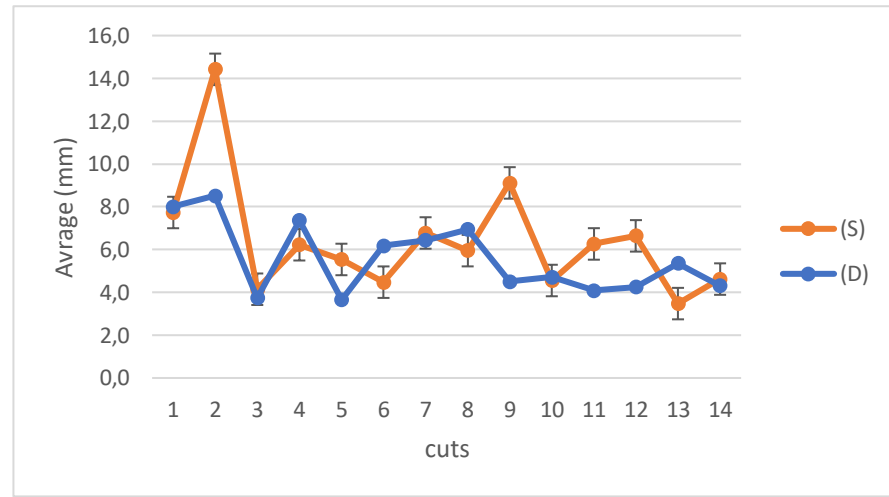


Figure 17. Distance average for diastolic and systolic phases.

To broaden the comparison spectrum, a second optical flow-based filter is tested. Thus, we present the result of the monitoring of the myocardial border points by the use of Lucas Kanade-Tomasi algorithm [66]. This standard algorithm uses spatial intensity information to orient and guide the search for the best matches. The objective of the KLT algorithm is to find the best alignment of the model with the distorted image by minimizing the sum of the squared errors between them. **Figure 18** shows the obtained results. The region of interest detected in the selected area is marked by the white "+" symbols, as shown. Subsequently, the point tracking system will follow the RV image by image. The detected point is marked by the green "+" symbol.

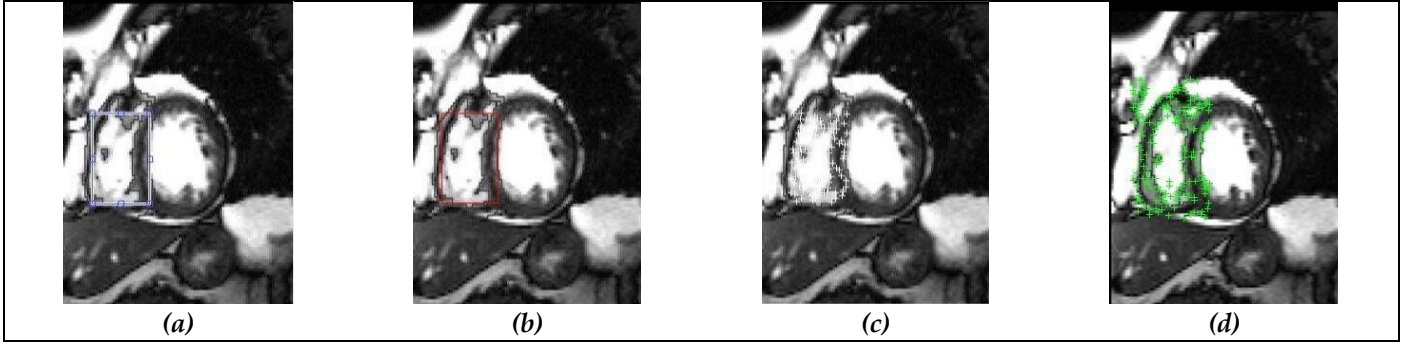


Figure 18. Applying Lucas Kanade-Tomasi (KLT) feature tracking method:(a) Selected region, (b) Red box shows region object, (c) Detected points of interest, (d) Selected points.

The algorithm was described on the basis of a point tracking system to recognize the RV myocardium. The input sequence used is grayscale and 240x280 in size, and it consists of approximately 14 frames as shown in **figure 19**. The filter appears to work properly as long as the slices are clear. If there is noise, the tracker gets lost and the edges are poorly detected.

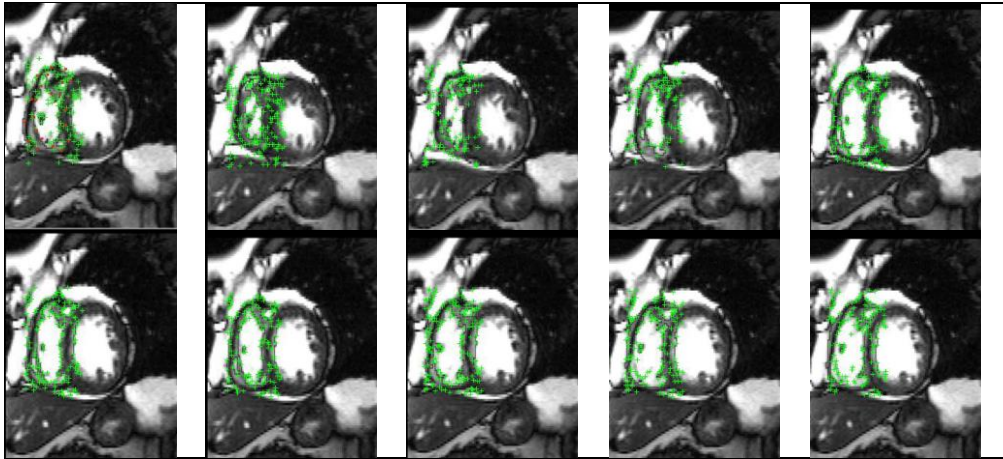


Figure 19. Estimated flow over the first ten cuts using Lucas Kanade-Tomasi (KLT) feature tracking method.

7. Conclusions

In this work, we initially proposed a segmentation method based on the topological transformation of the watershed line to detect the endocardial and epicardial contours. This segmentation was followed by the extraction of the right ventricular myocardium. Compared with conventional methods, the proposed approach is an efficient one since it ensures a faithful detection of ventricular contours. In addition to its preservation of topology, such segmentation provides a solid basis for calculating all parameters of right ventricular function such as ventricular mass, ejection fraction, ejection volume, and myocardial thickness as well as modeling the 3D volume. To perform motion tracking, a model adapted for temporal modeling of RV deformation is proposed. The periodicity assumption has been used to converge the Kalman filter. The proposed model was validated using an inter database of 20 patients. These data, which were anonymized, come from clinical exams performed at Fattouma Bourguiba University Hospital, Monastir, Tunisia. Indeed, the Kalman filter can be considered a powerful estimation and prediction tool when considering system modeling. Nevertheless, this filter is not necessarily a tool that can be applied in all cases. In fact, the system must be modeled accurately enough to design an effective filter. Additionally, this technique has lingering flaws. First, the covariance of the error does not necessarily converge.

Second, it causes a high computational cost. Another important limitation of such a method is that the Kalman filter allows considering only a Gaussian noise model while other types of noise need to be considered especially in image processing as Poisson noise. This restriction, therefore, limits the use of the Kalman filter.

Funding: This research received no external funding

Acknowledgments: A special thanks goes to the whole team of the radiology department of the Fattouma Bourguiba hospital in Monastir, Tunisia

Conflicts of Interest: The authors declare no conflict of interest

References

- [1] S. S. L. K., S. T. Ahmed, K. Anitha, and M. K. Pushpa, "COVID-19 Outbreak Based Coronary Heart Diseases (CHD) Prediction Using SVM and Risk Factor Validation," in *2021 Innovations in Power and Advanced Computing Technologies (i-PACT)*, 2021, pp. 1–5. doi: 10.1109/i-PACT52855.2021.9696656.
- [2] M. Chlabicz *et al.*, "A Similar Lifetime CV Risk and a Similar Cardiometabolic Profile in the Moderate and High Cardiovascular Risk Populations: A Population-Based Study," *JCM*, vol. 10, no. 8, p. 1584, Apr. 2021, doi: 10.3390/jcm10081584.
- [3] S. S. Thouheed Ahmed, K. Thanuja, N. S. Guptha, and S. Narasimha, "Telemedicine approach for remote patient monitoring system using smart phones with an economical hardware kit," in *2016 International Conference on Computing Technologies and Intelligent Data Engineering (ICCTIDE'16)*, 2016, pp. 1–4. doi: 10.1109/ICCTIDE.2016.7725324.
- [4] S. Sivalokanathan, "The Role of Cardiovascular Magnetic Resonance Imaging in the Evaluation of Hypertrophic Cardiomyopathy," *Diagnostics*, vol. 12, no. 2, p. 314, Jan. 2022, doi: 10.3390/diagnostics12020314.
- [5] S. Chillon, A. M. Mas, E. Schouman-Claeys, J. M. Serfaty, J. P. Laissy, and G. Pegon, "Etude de la fonction contractile du cœur en IRM," *Journal de Radiologie*, vol. 87, no. ue 10. 2006. doi: 10.1016/S0221-0363(06)86968-4.
- [6] A. K. Attili, A. Schuster, E. Nagel, J. H. Reiber, and R. J. Geest, "Quantification in cardiac MRI: advances in image acquisition and processing," *The international journal of cardiovascular imaging*, vol. 1, no. Suppl 1, pp. 27–40, 2010, doi: 10.1007/s10554-009-9571-x.
- [7] R. Mahmoudi *et al.*, "Left ventricular segmentation based on a parallel watershed transformation towards an accurate heart function evaluation," *IET Image Processing*, vol. 14, no. 3, pp. 506–517, Feb. 2020, doi: 10.1049/iet-ipr.2018.6379.
- [8] H. Sakly, R. Mahmoudi, M. Akil, M. Said, and M. Tagina, "Moving Towards A 5D Cardiac Model," *J Flow Vis Image Proc*, vol. 26, no. 1, pp. 19–48, 2019, doi: 10.1615/JFlowVisImageProc.2018027194.
- [9] A. Farb, A. P. Burke, and R. Virmani, "Anatomy and Pathology of the Right Ventricle (Including Acquired Tricuspid and Pulmonic Valve Disease)," *Cardiology Clinics*, vol. 10, no. 1, pp. 1–21, Feb. 1992, doi: 10.1016/S0733-8651(18)30252-2.
- [10] A. Chaturvedi, J. Whitnah, J. H. Maki, T. Baran, and L. M. Mitsumori, "Horizontal Long Axis Imaging Plane for Evaluation of Right Ventricular Function on Cardiac Magnetic Resonance Imaging," *Journal of clinical imaging science*, vol. 6, p. 52, 2016, doi: 10.4103/2156-7514.197076.
- [11] A. Ammari, R. Mahmoudi, B. Hmida, R. Saouli, and M. H. Bedoui, "A review of approaches investigated for right ventricular segmentation using short-axis cardiac MRI," *IET image process*, vol. 15, no. 9, pp. 1845–1868, Jul. 2021, doi: 10.1049/ipr2.12165.
- [12] A. Ammari, R. Mahmoudi, B. Hmida, R. Saouli, and M. H. Bedoui, "Slice-Level-Guided Convolutional Neural Networks to study the Right Ventricular Segmentation using MRI Short-Axis sequences," in *2021 IEEE/ACS 18th International Conference on Computer Systems and Applications (AICCSA)*, Tangier, Morocco, Nov. 2021, pp. 1–6. doi: 10.1109/AICCSA53542.2021.9686842.
- [13] K. Boukhris, R. Mahmoudi, A. B. Abdallah, M. AbdelAli, B. Hmida, and M. H. Bedoui, "U-Shaped Densely Connected Convolutions for Left Ventricle Segmentation from CMR Images," in *Computer Analysis of Images and Patterns*, vol. 13052, N. Tsapatsoulis, A. Panayides, T. Theodorides, A. Lanitis, C. Pattichis, and M. Vento, Eds. Cham: Springer International Publishing, 2021, pp. 145–153. doi: 10.1007/978-3-030-89128-2_14.
- [14] A. Elnakib, M. Ghazal, F. Taher, A. H. Mahmoud, and A. El-Baz, "Computational methods for identifying left ventricle heart pathologies," in *Diabetes and Cardiovascular Disease*, Elsevier, 2021, pp. 59–93. doi: 10.1016/B978-0-12-817428-9.00003-6.
- [15] N. Benameur *et al.*, "Parametric Methods for the Regional Assessment of Cardiac Wall Motion Abnormalities: Comparison Study," *Computers, Materials & Continua*, vol. 69, no. 1, pp. 1233–1252, 2021, doi: 10.32604/cmc.2021.016860.
- [16] F. Haddad, S. A. Hunt, D. N. Rosenthal, and D. J. Murphy, "Right ventricular function in cardiovascular disease, part I: Anatomy, physiology, aging, and functional assessment of the right ventricle," *Circulation*, vol. 117, no. 11, pp. 1436–1448, 2008, doi: 10.1161/CIRCULATIONAHA.107.653576.
- [17] M. S. Grewal and A. P. Andrews, *Kalman Filtering: Theory and Practice*. Englewood Cliffs, New Jersey: Prentice Hall, 1993.
- [18] S. W. Smith, *Digital Signal Processing*. Elsevier, 2003. doi: 10.1016/B978-0-7506-7444-7.X5036-5.
- [19] C. J. François, D. S. Fieno, S. M. Shors, and J. P. Finn, "Left ventricular mass: manual and automatic segmentation of true FISP and FLASH cine MR images in dogs and pigs," *Radiology*, vol. Feb;230(2):389-95, 2004, doi: 10.1148/radiol.2302020761.
- [20] A. Katouzian, A. Prakash, and E. Konofagou, "A New Automated Technique for Left- and Right-Ventricular Segmentation in Magnetic Resonance Imaging," in *International Conference of the IEEE Engineering in Medicine and Biology Society*, 2006, pp. 3074–3077. doi: 10.1109/IEMBS.2006.260405.

- [21] L. Zange *et al.*, "Quantification in cardiovascular magnetic resonance: agreement of software from three different vendors on assessment of left ventricular function, 2D flow and parametric mapping," *J Cardiovasc Magn Reson*, vol. 21, no. 1, p. 12, Dec. 2019, doi: 10.1186/s12968-019-0522-y.
- [22] R. J. Hemalatha, T. R. Thamizhvan, A. J. A. Dhivya, J. E. Joseph, B. Babu, and R. Chandrasekaran, "Active Contour Based Segmentation Techniques for Medical Image Analysis," in *Medical and Biological Image Analysis*, R. Koprowski, Ed. InTech, 2018. doi: 10.5772/intechopen.74576.
- [23] M. Kass, A. Witkin, and D. Terzopoulos, "Snakes: Active contour models," *Int J Comput Vision*, vol. 1, pp. 321–331, 1988, doi: 10.1007/BF00133570.
- [24] A. A. Amini, R. W. C. Yasheng Chen, V. Mani, and J. Sun, "Coupled B-snake grids and constrained thin-plate splines for analysis of 2-D tissue deformations from tagged MRI," *IEEE Transactions on Medical Imaging*, vol. 17, no. 3, pp. 344–356, Jun. 1998, doi: 10.1109/42.712124.
- [25] A. A. Young, D. L. Kraitchman, L. Dougherty, and L. Axel, "Tracking and finite element analysis of stripe deformation in magnetic resonance tagging," *IEEE Transactions on Medical Imaging*, vol. 14, no. 3, pp. 413–421, Sep. 1995, doi: 10.1109/42.414605.
- [26] P. Radeva, A. A. Amini, and J. Huang, "Deformable B-Solids and Implicit Snakes for 3D Localization and Tracking of SPAMM MRI Data," *Computer Vision and Image Understanding*, vol. 66, no. 2, pp. 163–178, May 1997, doi: 10.1006/cviu.1997.0611.
- [27] R. Mahmoudi and M. Akil, "Analyses of the Watershed Transform," *International Journal of Image Processing*, vol. 5, no. 5, pp. 521–541, 2011.
- [28] D. Mariano-Goulart, H. Collet, P.-O. Kotzki, M. Zanca, and M. Rossi, "Semi-automatic segmentation of gated blood pool emission tomographic images by watersheds: application to the determination of right and left ejection fractions," *European Journal of Nuclear Medicine and Molecular Imaging*, vol. 25, no. 9, pp. 1300–1307, Sep. 1998, doi: 10.1007/s002590050299.
- [29] Y. Lu, K. A. Connelly, A. J. Dick, G. A. Wright, and P. E. Radau, "Watershed segmentation of basal left ventricle for quantitation of cine cardiac MRI function," *J Cardiovasc Magn Reson*, vol. 13, no. S1, pp. P4, 1532–429X-13-S1-P4, Dec. 2011, doi: 10.1186/1532-429X-13-S1-P4.
- [30] S. D. Kamble, P. D. D., and S. Jagtap, "Morphological Image Segmentation by Morphological Watersheds," *Int J Recent Sci Res*, vol. 10, no. 01, pp. 30370–30374, 2019, doi: 10.24327/ijrsr.2019.1001.3045.
- [31] R. Mahmoudi, M. Akil, and M. H. Bedoui, "Concurrent computation of topological watershed on shared memory parallel machines," *Parallel Computing*, vol. 69, pp. 78–97, Nov. 2017, doi: 10.1016/j.parco.2017.08.010.
- [32] J. Cousty, G. Bertrand, L. Najman, and M. Couprie, "Watershed Cuts: Minimum Spanning Forests and the Drop of Water Principle," *IEEE Trans. Pattern Anal. Mach. Intell.*, vol. 31, no. 8, pp. 1362–1374, Aug. 2009, doi: 10.1109/TPAMI.2008.173.
- [33] A. Kornilov and I. Safonov, "An Overview of Watershed Algorithm Implementations in Open Source Libraries," *J. Imaging*, vol. 4, no. 10, p. 123, Oct. 2018, doi: 10.3390/jimaging4100123.
- [34] H. Fan, "Application of improved watershed image segmentation algorithm in post-processing of capacitive tomographic images," in *2020 IEEE International Conference on Artificial Intelligence and Information Systems (ICAIS)*, Dalian, China, Mar. 2020, pp. 485–489. doi: 10.1109/ICAIS49377.2020.9194796.
- [35] P. Devisivasankari and R. Vijayakumar, "Parallel Watershed method for Medical modality Image segmentation," in *2020 International Conference on Emerging Trends in Information Technology and Engineering (ic-ETITE)*, Vellore, India, Feb. 2020, pp. 1–3. doi: 10.1109/ic-ETITE47903.2020.407.
- [36] Q. Li and Y. Kang, "A Watershed-Based Intelligent Scissors Approach for Interactive Semi-Automated Pulmonary Lobes Segmentation," in *2020 International Conference on Machine Learning and Cybernetics (ICMLC)*, Adelaide, Australia, Dec. 2020, pp. 224–228. doi: 10.1109/ICMLC51923.2020.9469543.
- [37] A. Krishna, P. C. Srinivasa Rao, and C. M. A. K. Z. Basha, "Computerized Classification of CT Lung Images using CNN with Watershed Segmentation," in *2020 Second International Conference on Inventive Research in Computing Applications (ICIRCA)*, Coimbatore, India, Jul. 2020, pp. 18–21. doi: 10.1109/ICIRCA48905.2020.9183203.
- [38] J. Zhou, Y. Yin, and S. Wang, "Image Segmentation Based on Watershed Algorithm," in *2021 International Conference on Intelligent Computing, Automation and Applications (ICAA)*, Nanjing, China, Jun. 2021, pp. 10–13. doi: 10.1109/ICAA53760.2021.00010.
- [39] K. M. Farooqi *et al.*, "Application of Virtual Three-Dimensional Models for Simultaneous Visualization of Intracardiac Anatomic Relationships in Double Outlet Right Ventricle," *Pediatr Cardiol*, vol. 37, no. 1, pp. 90–98, Jan. 2016, doi: 10.1007/s00246-015-1244-z.
- [40] L. Tautz, L. Walczak, C. Manini, A. Hennemuth, and M. Hüllebrand, "3D Right Ventricle Reconstruction from 2D U-Net Segmentation of Sparse Short-Axis and 4-Chamber Cardiac Cine MRI Views," in *Statistical Atlases and Computational Models of the Heart. Multi-Disease, Multi-View, and Multi-Center Right Ventricular Segmentation in Cardiac MRI Challenge*, vol. 13131, E. Puyol Antón, M. Pop, C. Martín-Isla, M. Sermesant, A. Suinesiaputra, O. Camara, K. Lekadir, and A. Young, Eds. Cham: Springer International Publishing, 2022, pp. 352–359. doi: 10.1007/978-3-030-93722-5_38.
- [41] T. Küstner *et al.*, "CINENet: deep learning-based 3D cardiac CINE MRI reconstruction with multi-coil complex-valued 4D spatio-temporal convolutions," *Sci Rep*, vol. 10, no. 1, p. 13710, Dec. 2020, doi: 10.1038/s41598-020-70551-8.

- [42] T. J. W. Dawes *et al.*, "Machine Learning of Three-dimensional Right Ventricular Motion Enables Outcome Prediction in Pulmonary Hypertension: A Cardiac MR Imaging Study," *Radiology*, vol. 283, no. 2, pp. 381–390, May 2017, doi: 10.1148/radiol.2016161315.
- [43] K. Boukhris, R. Mahmoudi, B. Hmida, and M. H. Bedoui, "Accurate Left Ventricular Segmentation Based on Morphological Watershed Transformation Towards 3D Visualization," in *Digital Health in Focus of Predictive, Preventive and Personalised Medicine*, vol. 12, L. Chaari, Ed. Cham: Springer International Publishing, 2020, pp. 51–58. doi: 10.1007/978-3-030-49815-3_7.
- [44] F. Nascimento Martins and A. Santos Brandão, "Motion Control and Velocity-Based Dynamic Compensation for Mobile Robots," in *Applications of Mobile Robots*, E. Gorrostieta Hurtado, Ed. IntechOpen, 2019. doi: 10.5772/intechopen.79397.
- [45] N. Chleq and M. Thonnat, "Realtime image sequence interpretation for video-surveillance applications," in *Proceedings of 3rd IEEE International Conference on Image Processing*, 1996, vol. 2, pp. 801–804. doi: 10.1109/ICIP.1996.561026.
- [46] Akita, "Koichiro 'Image sequence analysis of real world human motion,'" *Pattern Recognition*, vol. 17, no. ue 1, pp. 73–83, 1984.
- [47] D. Koller, K. Daniilidis, and H. H. Nagel, "Model-based object tracking in monocular image sequences of road traffic scenes," *Int J Comput*, vol. 11263on 10, pp. 257–281, 1993, doi: 10.1007/BF01539538.
- [48] S. Wei and R. Jianxin, "Real-time Tracking of Non-rigid Objects," in *Proceedings of the 2016 International Conference on Communication and Information Systems (ICCIS '16, New York, NY, USA, 2016*, pp. 11–15. doi: 10.1145/3023924.3023944.
- [49] D. G. Lowe, "Three-dimensional object recognition from single two-dimensional images," *Artif. Intell*, vol. 31, 3, pp. 355–395, 1987, doi: 10.1016/0004-3702(87)90070-1.
- [50] K. ATIKA, "Image sequence analysis of real world human motion "," *Pattern Recognition*, vol. 17, no. ue 1, pp. 73–83, 1984.
- [51] Z. Chen and H. -J. Lee, "Knowledge-guided visual perception of 3-D human gait from a single image sequence," *IEEE Transactions on Systems, Man, and Cybernetics*, vol. 22, no. 2, pp. 336–342, Mar. 1992, doi: 10.1109/21.148408.
- [52] K. Rohr, "Towards model-based recognition of human movements in image sequences," *CVGIP: Image Underst*, vol. 59, 1, pp. 94–115, 1994, doi: 10.1006/ciun.1994.1006.
- [53] M. F. and B. P., "Region-based tracking in an image sequence," in *Computer Vision - ECCV'92. ECCV 1992. Lecture Notes in Computer Science*, vol. 588, G. Sandini, Ed. Berlin, Heidelberg: Springer, 1992. doi: 10.1007/3-540-55426-2_53.
- [54] J. Cousty, G. Bertrand, L. Najman, and M. Couprie, "Watershed Cuts: Thinnings, Shortest Path Forests, and Topological Watersheds," *IEEE Transactions on Pattern Analysis and Machine Intelligence*, vol. 32, no. 5, pp. 925–939, May 2010, doi: 10.1109/TPAMI.2009.71.
- [55] G. Bertrand, "Simple points, topological numbers and geodesic neighborhoods in cubic grids"," *Pattern Recognition Letters*, vol. 15, no. ue 10. 1994. doi: 10.1016/0167-8655(94)90032-9.
- [56] M. Couprie and G. Bertrand, "Topology preserving alternating sequential filter for smoothing two-dimensional and three-dimensional objects," *J. Electron. Imag*, vol. 13, no. 4, Oct. 2004, doi: 10.1117/1.1789986.
- [57] P. K. Gábor Németh and K. Palágyi., "Topology preserving parallel smoothing for 3d binary images," in *Proceedings of the Second international conference on Computational Modeling of Objects Represented in Images (CompIMAGE'10, Berlin, Heidelberg, 2010*, pp. 287–298. doi: 10.1007/978-3-642-12712-0_26.
- [58] R. Mahmoudi and M. Akil, "Enhanced computation method of topological smoothing on shared memory parallel machines," *J Image Video Proc.*, vol. 2011, no. 1, p. 16, Dec. 2011, doi: 10.1186/1687-5281-2011-16.
- [59] C. J. Clarke, M. J. Gurka, P. T. Norton, C. M. Kramer, and A. W. Hoyer, "Assessment of the Accuracy and Reproducibility of RV Volume Measurements by CMR in Congenital Heart Disease," *JACC: Cardiovascular Imaging*, vol. 5, no. 1, pp. 28–37, Jan. 2012, doi: 10.1016/j.jcmg.2011.05.007.
- [60] O. Bernard *et al.*, "Deep Learning Techniques for Automatic MRI Cardiac Multi-Structures Segmentation and Diagnosis: Is the Problem Solved?," *IEEE Trans. Med. Imaging*, vol. 37, no. 11, pp. 2514–2525, Nov. 2018, doi: 10.1109/TMI.2018.2837502.
- [61] J. Caudron, J. Fares, V. Lefebvre, P. H. Vivier, C. Petitjean, and J. N. Dacher, "Cardiac MRI assessment of right ventricular function in acquired heart disease: factors of variability," *Acad Radiol*, vol. Aug;19(8):991-1002, 2012, doi: 10.1016/j.acra.2012.03.022.
- [62] A. Ammari, R. Mahmoudi, B. Hmida, M. Mezri, R. Saouli, and M. Hédi Bedoui, "Clinical-Guided Strategy Towards a Spatio-Temporal Cardiac MRI Right Ventricular Short-Axis (ST-CMRI-RVSA) Labeled Dataset," *SN COMPUT. SCI.*, vol. 3, no. 4, p. 287, Jul. 2022, doi: 10.1007/s42979-022-01144-7.
- [63] Oumsis, M., Pham, QC., Sdigui, A.D., Neyran, B., Magnin, I.E. (2003). Modeling and Tracking of the Cardiac Left Ventricular Motion by a State Space Harmonic Model in MRI Sequence. In: Magnin, I.E., Montagnat, J., Clarysse, P., Nenonen, J., Katila, T. (eds) Functional Imaging and Modeling of the Heart. FIMH 2003. Lecture Notes in Computer Science, vol 2674. Springer, Berlin, Heidelberg. https://doi.org/10.1007/3-540-44883-7_19
- [64] Y. D. Zhu, M. Drangova, and N. J. Pelc, "Fourier tracking of myocardial motion using Cine-PC velocity data"," *Magnetic Resonance in Medicine*, vol. 35, pp. 471–480, 1996.
- [65] O. Ratib, B. Friedli, A. Righetti, and I. Oberhaensli, "Radionuclide evaluation of right ventricular wall motion after surgery in tertralogy of falot"," *Pediatric Cardiology*, vol. 10, pp. 25–31 1989.
- [66] B. D. Lucas and T. Kanade, "An Iterative Image Registration Technique with an Application to Stereo Vision," in *Proceedings of the 7th International Joint Conference on Artificial Intelligence - Volume 2, San Francisco, CA, USA, 1981*, pp. 674–679.